



Publication Year	2015
Acceptance in OA @INAF	2020-05-07T09:16:04Z
Title	Metal Deficiency in Cluster Star-Forming Galaxies At $Z = 2$
Authors	Valentino, F.; Daddi, E.; Strazzullo, V.; Gobat, R.; Onodera, M.; et al.
DOI	10.1088/0004-637X/801/2/132
Handle	http://hdl.handle.net/20.500.12386/24585
Journal	THE ASTROPHYSICAL JOURNAL
Number	801

METAL DEFICIENCY IN CLUSTER STAR-FORMING GALAXIES AT $Z = 2$ F. VALENTINO¹, E. DADDI¹, V. STRAZZULLO^{1,2}, R. GOBAT^{1,3}, M. ONODERA⁴, F. BOURNAUD¹, S. JUNEAU¹,
A. RENZINI⁵, N. ARIMOTO^{6,7}, M. CAROLLO⁴, AND A. ZANELLA¹¹ Laboratoire AIM-Paris-Saclay, CEA/DSM-CNRS-Université Paris Diderot, Irfu/Service d'Astrophysique,

CEA Saclay, Orme des Merisiers, F-91191 Gif sur Yvette, France; francesco.valentino@cea.fr

² Department of Physics, Ludwig-Maximilians-Universität, Scheinerstr. 1, D-81679 München, Germany³ School of Physics, Korea Institute for Advanced Study, Heogiro 85, Seoul 130-722, Korea⁴ Institute for Astronomy, ETH Zürich Wolfgang-Pauli-strasse 27, 8093 Zürich, Switzerland⁵ INAF-Osservatorio Astronomico di Padova Vicolo dell'Osservatorio 5, I-35122 Padova, Italy⁶ Subaru Telescope, National Astronomical Observatory of Japan 650 North A'ohoku Place, Hilo, HI 96720, USA⁷ Graduate University for Advanced Studies, 2-21-1 Osawa, Mitaka, Tokyo, Japan

Received 2014 October 4; accepted 2015 January 12; published 2015 March 12

ABSTRACT

We investigate the environmental effect on the metal enrichment of star-forming galaxies (SFGs) in the farthest spectroscopically confirmed and X-ray-detected cluster, CL J1449+0856 at $z = 1.99$. We combined *Hubble Space Telescope*/WFC3 G141 slitless spectroscopic data, our thirteen-band photometry, and a recent Subaru/Multi-object InfraRed Camera and Spectrograph (MOIRCS) near-infrared spectroscopic follow-up to constrain the physical properties of SFGs in CL J1449+0856 and in a mass-matched field sample. After a conservative removal of active galactic nuclei, stacking individual MOIRCS spectra of 6 (31) sources in the cluster (field) in the mass range $10 \leq \log(M/M_\odot) \leq 11$, we find a $\sim 4\sigma$ lower $[\text{N II}]/\text{H}\alpha$ ratio in the cluster than in the field. Stacking a subsample of 16 field galaxies with $\text{H}\beta$ and $[\text{O III}]$ in the observed range, we measure an $[\text{O III}]/\text{H}\beta$ ratio fully compatible with the cluster value. Converting these ratios into metallicities, we find that the cluster SFGs are up to 0.25 dex poorer in metals than their field counterparts, depending on the adopted calibration. The low metallicity in cluster sources is confirmed using alternative indicators. Furthermore, we observe a significantly higher $\text{H}\alpha$ luminosity and equivalent width in the average cluster spectrum than in the field. This is likely due to the enhanced specific star formation rate; even if lower dust reddening and/or an uncertain environmental dependence on the continuum-to-nebular emission differential reddening may play a role. Our findings might be explained by the accretion of pristine gas around galaxies at $z = 2$ and from cluster-scale reservoirs, possibly connected with a phase of rapid halo mass assembly at $z > 2$ and of a high galaxy merging rate.

Key words: galaxies: clusters: individual (CL J1449+0856) – galaxies: star formation – ISM: abundances

1. INTRODUCTION

The evolution of galaxies is regulated by the complex interplay of multiple physical mechanisms. Distinguishing the influence of external environmental effects from internal factors is crucial to reach a comprehensive understanding of these systems. From this perspective, galaxy clusters offer the perfect occasion to disentangle this situation, comparing samples of field and extreme overdensity galaxies at fixed mass. In the local universe, the influence of the strongest overdensities is manifest in well-known relations, such as the systematic variation of morphological type, luminosity, surface brightness, star formation rate (SFR), and colors with density (e.g., Dressler 1980; Gómez et al. 2003; Baldry et al. 2004; Balogh et al. 2004; Hogg et al. 2004; Blanton et al. 2005). As a result, local virialized and massive clusters are centrally dominated by massive, red, and passive early-type galaxies, while blue star-forming galaxies (SFGs) are preferentially located in the cluster outskirts and in the field. A key to deciphering the origin of the observed local environmental trends is the study of high redshift cluster galaxies as compared to the field. Unlike the extended and increasing statistics of well-studied clusters at $z < 1.5$ in the literature, only a handful of clusters above this redshift have been confirmed today (e.g., Andreon et al. 2009; Papovich et al. 2010; Fassbender et al. 2011; Gobat et al. 2011; Santos et al. 2011; Stanford et al. 2012; Zeimann et al. 2012; Muzzin et al. 2013). Studying the redshift interval above $z > 1.5$ is crucial as we approach the era when the first

massive clusters begin to emerge and an epoch where galaxies were still assembling a large fraction of their stellar mass through active star formation (Daddi et al. 2007). In addition to the low statistics, the mentioned properties which designate an evolved cluster at $z = 0$ become progressively blurred at increasing redshift, making it difficult to fully characterize the evolutionary stage of overdensities and, consequently, to quantify their effect on galaxy evolution. Despite these difficulties, sustained efforts have been, and continue to be, made to detect, confirm, and characterize high-redshift clusters. In particular, the recent dramatic improvement in near-infrared (near-IR) multi-object spectrographs has opened the door to the study of the physical properties of ionized gas in SFGs through a set of emission lines that have been well studied in local objects, such as $\text{H}\beta$, $[\text{O III}]\lambda 5007$ (hereafter $[\text{O III}]$), $\text{H}\alpha$, and $[\text{N II}]\lambda 6584$ (hereafter $[\text{N II}]$). These lines also provide access to the gas-phase metallicity in SFGs, if properly calibrated. A mass-metallicity relation (MZR) has been shown to be in place from $z = 0$ (Tremonti et al. 2004) up to a redshift of $\sim 3\text{--}4$ (Savaglio et al. 2005; Erb et al. 2006; Troncoso et al. 2014; Zahid et al. 2014b; Wuyts et al. 2014, and others), indicating that more massive galaxies are also more metal-rich at almost any epoch. As recent modeling suggests (e.g., Davé et al. 2012; Lilly et al. 2013), this relation may result from secular metal enrichment of the gas through stellar winds from young stars, modulated by galactic outflows and inflows and by the formation of a subsequent generation of stars. At increasing

redshift, the gas-phase metallicity in SFGs is observed to decrease, but our knowledge of possible effects of the surrounding environment on metal enrichment is still uncertain. In the local universe, the environmental effect seems to be limited, if at all present (Mouhcine et al. 2007; Cooper et al. 2008; Ellison et al. 2009; Hughes et al. 2013), and recent studies at high redshifts have focused only on few protoclusters at $z > 2$ (Kulas et al. 2013; Shimakawa et al. 2015). In this work, we present results relative to the farthest spectroscopically confirmed X-ray detected cluster discovered to date, CL J1449+0856 at $z = 1.99$ (Gobat et al. 2011, 2013, hereafter G11, G13). As indicated by the presence of a dominant population of red, massive, and passive galaxies in its core (Strazzullo et al. 2013, hereafter S13), and coupled with the X-ray detection, CL J1449+0856 is in a relatively evolved phase compared with other known structures at the same epoch, making it the potential progenitor of a massive local cluster (G11). These features physically distinguish this overdensity from lower halo mass, SFG dominated, rapidly assembling protoclusters at similar or higher redshifts (e.g., Steidel et al. 2005; Kodama et al. 2013) and potentially these intrinsically different structures may give rise to different effects on their host galaxies. We present here a recent Subaru/Multi-object InfraRed Camera and Spectrograph (MOIRCS) follow-up of the star-forming population in CL J1449+0856, for which we primarily measured $H\alpha$ and $[N II]$ emission lines. Incorporating previous information about $[O III]$ and $H\beta$ from *Hubble Space Telescope* (HST)/WFC3 G141 slitless spectroscopy (G13), we can estimate the metallicity through the $N2 = \log([N II]/H\alpha)$ and $O3N2 = \log([O III]/H\beta)/([N II]/H\alpha)$ indicators (Alloin et al. 1979), exploring different calibrations proposed in recent literature (Pettini & Pagel 2004; Steidel et al. 2014). We compare the MZR and other interstellar medium (ISM) properties of SFGs in CL J1449+0856 with a mass-matched field sample at comparable redshift, allowing for a direct probe of the environmental effects of relatively evolved overdensities on SFGs at $z = 2$.

This paper is organized as follows. In Section 2, we describe the sample selection and the near-IR spectroscopic and ancillary data used for the analysis. In Section 3, we present the full photometric and spectroscopic analysis of the data set along with the derived ISM physical condition through currently used line diagnostic diagrams. We show the results about the MZR in Section 4 and we discuss potential implications in Section 5. Section 6 summarizes the main findings of this work. Additional technical remarks are reported in the Appendix. Throughout the paper we adopt a flat Λ CDM cosmology with $\Omega_m = 0.3$, $\Omega_\Lambda = 0.7$ and $H_0 = 70 \text{ km s}^{-1} \text{ Mpc}^{-1}$, and a Salpeter initial mass function (IMF, Salpeter 1955). When necessary we converted results from literature obtained with other IMFs to a Salpeter IMF.

2. DATA AND SAMPLE SELECTION

Galaxy populations in CL J1449+0856 were investigated in G11, G13, and S13. The cluster is spectroscopically confirmed with currently 27 members identified with Very Large Telescope/VIMOS and FORS2, and WFC3 spectroscopy (G11, G13). Most spectroscopic redshifts in the field of CL J1449+0856 come from the WFC3 G141 spectroscopic follow-up (Figure 1), with 140 redshift determinations over a $\sim 4 \text{ arcmin}^2$ area, based on emission lines (typically $[O II] \lambda 3727$, $[Ne III]$, $H\beta$, $[O III]$ at $z \sim 2$) or on continuum breaks in

the spectral range $1.1\text{--}1.7 \mu\text{m}$ (full details can be found in G13). These include 68 $[O III]$ emitters, 17 of which belong to the cluster. CL J1449+0856 was also imaged at wavelengths from X-ray to radio (G13). In this work, we used the same photometric catalogs as in S13, including optical/NIR photometry in 13 passbands from U to $4.5 \mu\text{m}$. Sources were detected in the WFC3/F140W band, and photometry was measured with SExtractor (Bertin & Arnouts 1996), as well as with GALFIT (Peng et al. 2002, 2010) modeling. Based on photometric redshifts determined on such photometry, a sample of candidate cluster members was identified in the cluster's central region, virtually complete at $M \gtrsim 10^{10} M_\odot$, although affected by significant contamination especially below $10^{10} M_\odot$. Galaxies were also broadly classified as “passive” or “star-forming” based on restframe UVJ colors (Wuyts et al. 2007; Williams et al. 2009) and spectral energy distribution fitting (SED, S13). In this work, we focus on SFGs in the mass range of $10 \leq \log(M/M_\odot) \leq 11$. The full sample of cluster galaxies in the F140W-based catalog includes six spectroscopically confirmed and two candidate star-forming cluster members in this mass range.

For our MOIRCS near-IR follow-up, we selected a sample of 110 objects. These included 76 sources in CL 1449+0856 field, where we gave the highest priority to WFC3 spectroscopically confirmed star-forming members (10 objects: 2 with $M < 10^{10} M_\odot$, 6 with $10^{10} M_\odot \leq M \leq 10^{11} M_\odot$, and 2 with $M > 10^{11} M_\odot$) and to star-forming objects from the pool of candidate members according to their probability of belonging to the cluster (S13) and irrespectively of their mass. We note here that cluster SFGs were not specifically selected to be $[O III]$ emitters. The two candidates in the mass range of $10 \leq \log(M/M_\odot) \leq 11$ were not observed due to geometrical constraints in slit positioning. In the area covered by WFC3, we selected 13 $[O III]$ emitters that did not belong to the overdensity, which became part of the field control sample at $z \sim 2$. Outside the WFC3 field, where no spectroscopy was available, we selected field objects with $z_{\text{phot}} \geq 2$ with the highest chances to detect $H\alpha$, i.e., with an estimated $H\alpha$ flux $\geq 3 \times 10^{-17} \text{ erg cm}^{-2} \text{ s}^{-1}$ from the SED-based SFR and reddening estimates (see Section 3). Finally, to further extend our field control sample, we observed 34 BzK -SFGs (Daddi et al. 2004) with $z_{\text{phot}} \sim 2$ with an estimated $H\alpha$ flux $\geq 3 \times 10^{-17} \text{ erg cm}^{-2} \text{ s}^{-1}$ in the COSMOS field (Scoville et al. 2007). A posteriori, the predicted $H\alpha$ was $\sim 25\%$ lower than the measured flux for these field $H\alpha$ -selected sources, probably due to Malmquist bias. We note here that, even if the total integration time over the COSMOS field is shorter than over the cluster field, this does not substantially impact the main results of this work, based on the stacking of sources (see Section 3.2). The objects in the COSMOS field contributed to $\sim 30\%$ of the total number of field sources in the final stacked spectrum (10/31) and reached $H\alpha$ fluxes comparable to the dimmest sources in CL 1449+0856 field (3.2×10^{-17} and $3.3 \times 10^{-17} \text{ erg cm}^{-2} \text{ s}^{-1}$ at $>5\sigma$ in the cluster and COSMOS field, respectively).

2.1. Subaru/MOIRCS Spectroscopy

We carried out near-IR spectroscopy with MOIRCS at the Subaru Telescope (Ichikawa et al. 2006). Two Hawaii-2 2048 \times 2048 detectors cover the $4' \times 7'$ FoV and up to 40 slits can be placed within the inner $6'$ diameter circular region. We used the HK500 grism with $0.7''$ wide slits, which provides a

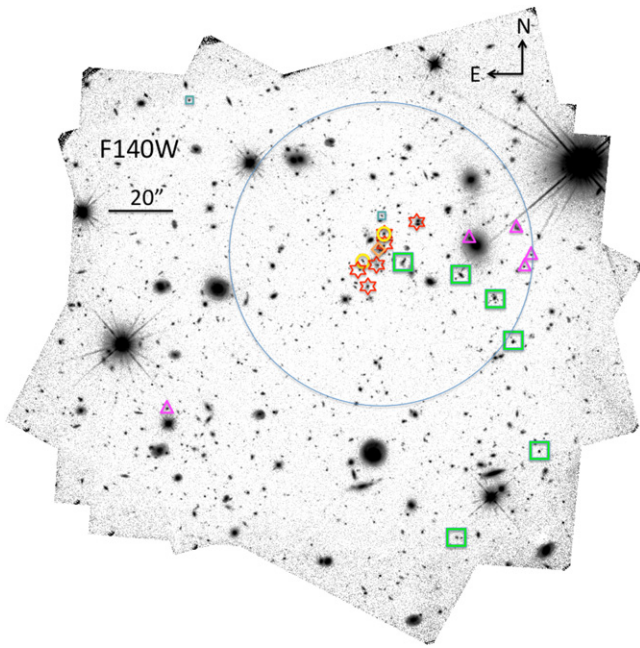


Figure 1. Deep F140W image of CL J1449+0856 and its spectroscopically confirmed members in the field observed with WFC3 (G13). Red stars mark passive galaxies. Yellow circles indicate X-ray detected AGNs. Green squares indicate SFGs in the mass range of $10 \leq \log(M/M_{\odot}) \leq 11$ and blue squares indicate SFGs in the mass range of $\log(M/M_{\odot}) < 10$, both targeted and detected with MOIRCS. Purple triangles indicate other SFGs not targeted with MOIRCS. The orange diamond shows the assembling brightest central galaxy. The blue solid circle represents the putative $R_{200} \sim 0.4$ Mpc radius (physical, G13).

resolving power of $R \simeq 500$ along the 13000–23000 spectral range. A total of three masks were designed, two for the CL J1449+0856 field and one for the COSMOS field. The observations were carried out in a single run on three consecutive nights in 2013 April. A sequence of 600s integrations was taken with a standard ABAB 1/5 dithering pattern. Calibration frames of an A0V standard star and dome flat fields were taken at either the beginning or the end of each night. We integrated the images for a total of 7.3, 6.7, and 3.4 hr on 38, 38, and 34 galaxies for Mask 1 and 2 on CL J1449+0856 and Mask 3 in the COSMOS field, respectively, with a mean seeing of ~ 0.6 during three clear nights. The observation plan is summarized in Table 1.

We reduced the data with the MCSMDP pipeline⁸ (Yoshikawa et al. 2010) combined with custom IDL scripts. First, the data were flat-fielded employing dome-flat frames collected in the same configuration of science frames, and bad pixels and other detector defects were removed using masks provided in the pipeline. Then, cosmic rays were removed by combining each A frame with the corresponding dithered B image. The sky subtraction was automatically performed subtracting each B frame to the corresponding A image. Then the distortion introduced by the detectors was corrected using the coefficients used in the MOIRCS imaging reduction package. Each 2D spectrum was then cut from every global frame and wavelength calibrated on a grid of bright OH-airglow lines (Rousselot et al. 2000), with an uncertainty of half a pixel, i.e., ~ 3.5 . We co-added all of the 2D spectra, down-weighting the frames taken in worse atmospheric conditions to minimize the effect of

Table 1
Observation Log

Mask ID ^a	Date ^b	Integration time ^c (hr)	Target field ^d
Mask 1	2013 Apr, 7th	4.3	CL J1449+0856
	2013 Apr, 9th	3	CL J1449+0856
Mask 2	2013 Apr, 8th	5	CL J1449+0856
	2013 Apr, 9th	1.7	CL J1449+0856
Mask 3	2013 Apr, 7th	1.7	COSMOS
	2013 Apr, 8th	1.2	COSMOS
	2013 Apr, 9th	0.5	COSMOS

Notes.

^a ID of the three MOIRCS masks.

^b Date of observation.

^c Total integration time per night.

^d Pointed target field.

variable seeing during the observing run. We finally extracted the 1D spectra and flux-calibrated them by comparing with a standard A0V stellar spectrum. We estimated aperture corrections (~ 1.3 on average) comparing the integrated flux within the H and Ks bands with the total photometric values. As a final step, we modeled the noise at each wavelength, taking into account possible slit-to-slit and wavelength-dependent sky variations.

We successfully detected (3σ confidence level down to an observed $H\alpha$ flux of 1.4×10^{-17} erg cm⁻² s⁻¹) at least one line in 71% of the sample (78/110 galaxies). In 71, 22, 41, and 7 galaxies we detected at 3σ $H\alpha$, $[N II]$, $[O III]$, and $H\beta$, respectively. For galaxies where we detected at least one line at 3σ , we put 2σ upper limits on the other lines, if present in the observed spectral range. When available, we averaged the line fluxes from WFC3 observations with MOIRCS-detected lines, assigning higher weights to higher signal-to-noise ratio (S/N) estimates and properly taking into account the consistency of the $[O III]/H\beta$ ratios and the total flux scaling between the two independent measurements. A total of 49 galaxies have a detection or a 2σ upper limit on all $H\beta$, $[O III]$, $H\alpha$, $[N II]$ emission lines.

3. METHODOLOGY

3.1. SED Fitting

Stellar masses, SFRs, and dust reddening were determined using FAST (Kriek et al. 2009) on the UV to IR photometry. We used Bruzual & Charlot (2003) models with constant star formation histories (SFHs) and a Salpeter IMF (Salpeter 1955). The Calzetti et al. (2000) reddening law was used to estimate the extinction. For the COSMOS sample, for which the photometric coverage probes the rest-frame UV SED with high accuracy, we allowed for a variable UV bump in the fit (Noll et al. 2009). The slope of the attenuation law was not fitted and the derived SFR estimates are consistent with those derived with the Calzetti et al. (2000) law. We note that the choice of a different SFH, possibly rising or exponentially declining, negligibly affects our mass estimates, well within systematic uncertainties (~ 0.2 dex). Indeed, for active SFGs at these redshifts, the SED fit gives in most cases very short ages and comparable e -folding times, such that the actual SFH is nearly constant whether or not an exponentially increasing or decreasing SFR is used (Maraston et al. 2010). On the

⁸ <http://www.naoj.org/Observing/DataReduction/>

Table 2
Properties of the Six Confirmed Cluster Star-forming Members in the Stack

ID	R.A. (deg)	Decl. (deg)	z_{spec}	$\log(M)$ ($\log(M_{\odot})$)	$E(B - V)_{\text{neb}}^{\text{SED}^a}$	$\text{SFR}_{\text{H}\alpha}$ ($M_{\odot} \text{ yr}^{-1}$)
ID568	222.3024796	8.9387313	1.987 ± 0.001	10.38	0.33	118 ± 9^b
ID510	222.2997850	8.9369198	1.988 ± 0.001	10.52	0.53	158 ± 13
ID422	222.2983118	8.9335256	1.988 ± 0.001	10.53	0.43	361 ± 60
ID183	222.2961999	8.9248673	1.990 ± 0.001	10.05	0.10	24 ± 3
ID580	222.3070938	8.9397864	2.001 ± 0.001	10.54	0.43	189 ± 23
ID41	222.3029800	8.9186500	1.991 ± 0.001	10.63	0.50	125 ± 30

Notes.

^a $E(B - V)_{\text{neb}}^{\text{SED}}$ is the nebular reddening derived from the SED modeling as $E(B - V)_{\text{cont}}/f$ (Section 3.3.3).

^b ID568 shows peculiar WFC3 emission line maps (Zanella et al. 2015). Using the emission line maps to compute the aperture correction and the reddening prescription from Zanella et al. (2015) would lead to $\text{SFR}_{\text{H}\alpha} = 77 \pm 9 M_{\odot} \text{ yr}^{-1}$.

contrary, other parameters used in this work are potentially affected by the choice of the SFH, e.g., the SFR. We opted for a constant SFH as it proved to give consistent results in representing the so-called “Main Sequence” of SFGs (MS, Daddi et al. 2007; Rodighiero et al. 2014), matching the SFRs derived independently from H α fluxes and FIR and X-ray stacking. We fitted the photometry for both the aperture-based and the GALFIT-based catalogs (see Section 2 and S13). Stellar masses and SFRs from the SExtractor catalog were corrected based on total-to-aperture flux ratios ($\lesssim 0.15$ dex for the sample used here). For those galaxies for which the IRAC photometry suffers from a potentially heavy contamination from neighbors ($\sim 10\%$ of our sample), we excluded the 3.6–4.5 μm bands from the fitting procedure. The two photometric catalogs yield broadly consistent parameter values (e.g., a ~ 0.1 dex difference in total stellar masses).

3.2. Stacking

In order to maximize the information derivable from the observed spectra and to find an average trend for the cluster and field samples, we stacked individual spectra. We blueshifted the spectra to the rest-frame and registered them on a common grid of ~ 2.7 and ~ 3.7 step for the cluster and field, respectively. Then for every wavelength step we averaged the flux values, weighting for the inverse variance if a sufficiently high number of spectra were co-added ($N > 10$). On the other hand, a straight mean was computed in stacking a low number of spectra ($N < 10$), not to introduce wavelength dependent biases. We note here that averaging individual spectra does not necessarily coincide with averaging spectral derived quantities. The difference between these two averaged trends depends on the relationship between line fluxes and the derived quantities. In our case, we estimated the impact of this difference on the mean metallicity calculated through the line ratio $[\text{N II}]/\text{H}\alpha$ for a population of MS–SFGs. For masses of $M \geq 10^{10} M_{\odot}$, considering the low number statistics for the cluster sample, the two computed averages are similar ($< 4\%$ difference). Therefore, we adopted the mean metallicities coming from the stacking procedure as representative of the population without applying any other correction. The details of this calculation are reported in the Appendix.

Considering the low number of sources with $\log(M/M_{\odot}) < 10$ and $\log(M/M_{\odot}) > 11$, we opted for stacking all galaxies with a spectroscopic redshift determination and H α coverage in the mass range of $10 \leq \log(M/M_{\odot}) \leq 11$. To investigate possible environmental effects, we stacked the

cluster and field sources separately, after a conservative active galactic nuclei (AGNs) removal (see Section 3.3.1). We stacked six sources without implementing any weighting scheme for the cluster sample at $z = 1.99$ (Table 2). In the same mass bin, we stacked 31 field sources ($\langle z \rangle = 1.92$) with H α and $[\text{N II}]$ in the observed range and a subsample of 16 galaxies ($\langle z \rangle = 2.14$) with H β and $[\text{O III}]$ in addition. Given the number of objects, we applied the optimal weighting described above to the field sample. Unless noted otherwise, in the rest of this work, we will use the 31 sources field stack as a main term of comparison for the analysis of environmental effects to exploit at maximum the sample observed with MOIRCS and we refer to it as the “field stack.” However, we made use of the 16-source stacked subsample when necessary, i.e., when $[\text{O III}]$ or H β fluxes were required. The $[\text{N II}]/\text{H}\alpha$ ratio in the 31-source and 16-source field stacks is consistent within the uncertainties. The stacked spectra are shown in Figures 2 and 3, and their photometric and spectroscopic properties are summarized in Tables 3 and 4. In Figure 4, we plot the continuum-subtracted stacked spectra normalized to their H α total fluxes. Furthermore, we checked if the brightest H α emitters biased the average spectra, stacking individual sources normalized by their observed and intrinsic H α fluxes. In both cases, $[\text{N II}]/\text{H}\alpha$ and $[\text{O III}]/\text{H}\beta$ are fully compatible with the non- and optimally weighted measurements within 1σ error bars. We also stacked only five cluster sources at a time to check for the impact of low number statistics. In all the cases, $[\text{N II}]/\text{H}\alpha$ and $[\text{O III}]/\text{H}\beta$ ratios are consistent within 1σ with the non-weighted measurements, except for the $[\text{O III}]/\text{H}\beta$ ratio when stacking only the upper limits on $[\text{N II}]$ (in this case, the ratio varies within 2σ error bars, suggesting possible important physical variance within the sample). We note here that among the six cluster sources in the stack, only the brightest one in H α is detected in $[\text{N II}]$ at 2σ and corresponds to the lowest $[\text{N II}]/\text{H}\alpha$ ratio, which is nevertheless consistent with the average value for the remaining five cluster sources. Therefore, the $[\text{N II}]$ detection is likely the effect of the bright H α emission. Finally, all six cluster SFGs in the $10 \leq \log(M/M_{\odot}) \leq 11$ mass range have a WFC3 spectrum, and for 5/6 sources the 3600–5700 rest-frame interval is covered, giving access to the $[\text{O II}]\lambda 3727$ emission line ($[\text{O II}]$ in the following). Hence, we stacked the WFC3 spectra as done for MOIRCS spectra, rescaling to match the absolute fluxes from broadband photometry. The final stacked $[\text{O III}]$ and H β fluxes from the WFC3 and MOIRCS spectra result fully compatible within the uncertainties.

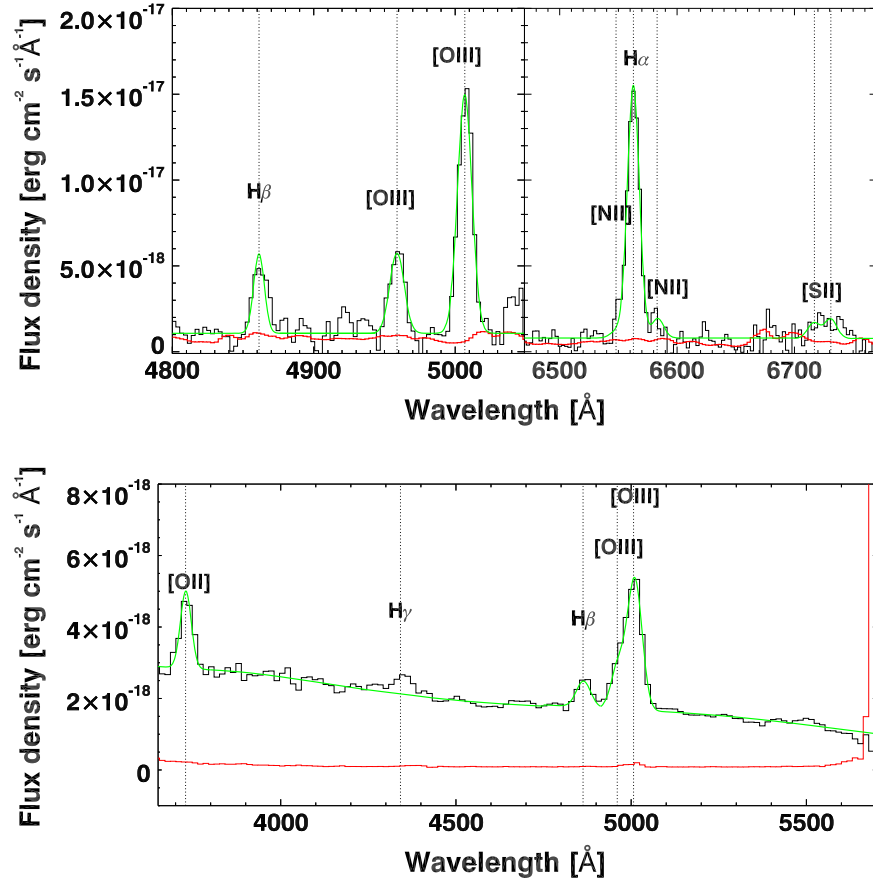


Figure 2. MOIRCS (top panel) and WFC3 (bottom panel) stacked spectra and noise of the sample of six cluster SFGs in the mass range of $10 \leq \log(M/M_{\odot}) \leq 11$. The black and red lines, respectively, represent the stacked spectra and noise. The green line shows the best fit for the emission lines. Vertical dotted lines mark the expected location of emission lines of interest, as labeled.

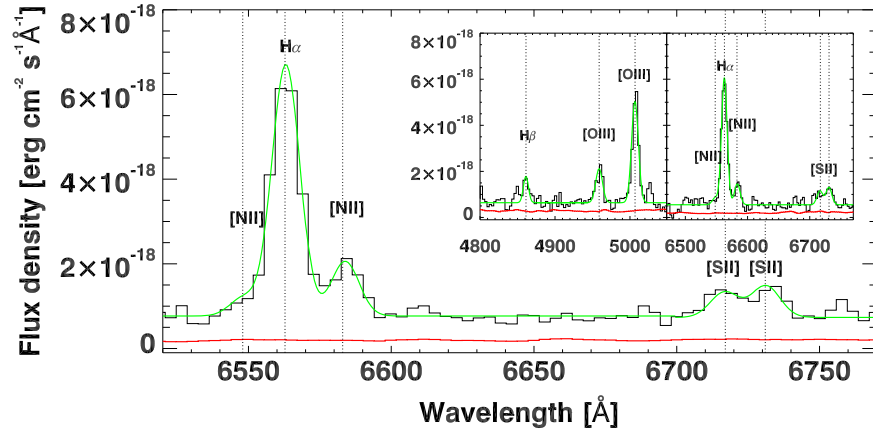


Figure 3. MOIRCS stacked spectrum and noise of the sample of 31 field SFGs in the mass range $10 \leq \log(M/M_{\odot}) \leq 11$ with $H\alpha$ and $[N II]$ in the observed wavelength range. The black and red lines, respectively, represent the stacked spectrum and noise. The green line shows the best fit for the emission lines. The inset shows the MOIRCS stacked spectrum and noise for the subsample of 16 field SFGs in the same mass range with $H\beta$, $[O III]$, $H\alpha$, and $[N II]$ in the observed wavelength range. Vertical dotted lines mark the expected location of emission lines of interest, as labeled.

3.3. Line Fluxes

We measured line fluxes fitting Gaussian profiles to the emission lines on flux calibrated and aperture corrected spectra. We used the squared inverse of the noise array to weigh the fitting and to estimate the errors on total fluxes and line positions and thus on the redshift determination. Using the IDL script MPFIT (Markwardt 2009), at the same time, we fitted three Gaussian profiles lying on a flat continuum to measure

$[N II] \lambda\lambda 6548, 6583$ and $H\alpha$ fluxes. We modeled the local continuum around each emission line in wavelength ranges large enough to be dominated by continuum emission (~ 1000). In the very few cases where a flat continuum did not provide a good model, we fitted a polynomial curve. We left the $H\alpha$ central wavelength and FWHM free to vary in the fit, while we fixed the $[N II]$ doublet lines to share a common line width value set by $FWHM(H\alpha)$ (in terms of velocity), their expected positions relatively to $H\alpha$, and their flux ratio to 3.05 (Storey &

Table 3
Stacked Spectra Properties

Environment	No. sources	$\langle z \rangle$	$\log(M)$ ($\log(M_\odot)$)	SFR_{SED} ($M_\odot \text{ yr}^{-1}$)	$E(B - V)_{\text{cont}}$	$\text{SFR}_{\text{H}\alpha}$ ($M_\odot \text{ yr}^{-1}$)	$E(B - V)_{\text{neb}}$
Cluster	6	1.99	10.47	101	0.29	112	0.32
Field	31	1.92	10.57	126	0.31	68	...
Field	16	2.14	10.52	110	0.33	75	0.48

Note. SED derived quantities are the mean values of single sources in the stacked spectra.

Table 4
Stacked Spectra Observed Fluxes

Environment	No. sources	[O II] (cgs)	H β (cgs)	[O III] (cgs)	H α (cgs)	[N II] (cgs)	[S II] _{tot} ^a (cgs)
Cluster	6	0.800 ± 0.065^b	0.463 ± 0.065	1.781 ± 0.043	1.915 ± 0.061	0.145 ± 0.048	0.119 ± 0.026
Field	31	0.754 ± 0.020	0.159 ± 0.015	0.075 ± 0.011
Field	16	...	0.128 ± 0.016	0.499 ± 0.019	0.645 ± 0.016	0.104 ± 0.012	0.070 ± 0.010

Notes. The observed line fluxes are expressed in units of $10^{-16} \text{ erg cm}^{-2} \text{ s}^{-1}$. [O II] fluxes come from WFC3 observations (G13).

^a Total combined flux of [S II] $\lambda\lambda 6716, 6731$.

^b Value for 5/6 cluster members with [O II] coverage.

Zeppen 2000). Similarly, we simultaneously fitted the [O III] $\lambda\lambda 4959, 5007$ lines, fixing their position and width according to H α values and their intensity ratio to 2.98. Any other line in the observed range, both single or in multiplets, was fitted following the same procedure. We estimated flux uncertainties with MPFIT and rescaled them according to the χ^2 value when $\chi^2 > 1.5$. In addition, we ran Monte Carlo simulations, placing mock lines in empty spectral regions, recovering consistent uncertainties within $\sim 5\%$, confirming the reliability of our noise estimate. We finally estimated the H α and H β stellar absorption measuring the continuum at the proper wavelengths and assuming absorption equivalent widths $\text{EW}_{\text{H}\alpha}^{\text{abs}} = 3.5$ and $\text{EW}_{\text{H}\beta}^{\text{abs}} = 5$, as estimated from SED modeling. This correction is $\lesssim 15\%$ and $\sim 30\%$ for H α and H β , respectively.

3.3.1. Line Diagnostics Diagrams

Following the pioneering work by Baldwin et al. (1981), many studies have shown that the proper combination of ratios of collisionally excited and recombination lines can provide useful information not only about the element abundances in the gas in galaxies, but also about its ionization state and the primary ionizing source (e.g., Kewley & Dopita 2002; Kewley et al. 2013a). In this work, we investigate the gas state using the [N II]/H α –[O III]/H β diagram, commonly referred to as the BPT diagram. This can be used to distinguish line-emitting galaxies mainly powered by an AGN from those dominated by star formation: the radiation field emitted by the disk accreting around an AGN is harder, increasing the oxygen and nitrogen ionization and producing larger [O III] and [N II] fluxes with respect to the values reached by SF-powered ionization. However, the situation may be considerably different at higher redshifts: an evolution of the electron density, the ionization parameter, or the hardness of the radiation field can shift the locus of the SF sequence. Recent developments in multi-object near-IR spectroscopy have allowed for the observation of an increasing number of samples of line emitters, extending the study of the potential evolution of line ratios with cosmic time (e.g., Kewley et al. 2013a; Holden et al. 2014) and the role of

selection effects (Juneau et al. 2014) to earlier epochs, up to $z \geq 1.5$. Recent results by Steidel et al. (2014, S14 in the following) for a sample of $z \sim 2.3$ SFGs point toward a substantial vertical shift in the BPT diagram due to a harder field ionizing the ISM, qualitatively in agreement with some theoretical expectations (Kewley et al. 2013a, 2013b; but see, e.g., Coil et al. 2014; Shapley et al. 2014 for alternative results). Interestingly, S14 interpret the locus of SFGs mainly as an “ionization parameter” sequence, in contrast to the usual interpretation of a “gas-phase metallicity” sequence given in the local universe (Kewley & Ellison 2008). Figure 5 shows our sample in the BPT diagram and a reference sample at $z \sim 1.55$ from the Subaru/FMOS survey (Zahid et al. 2014b). A low-redshift ($0.04 < z < 0.2$) sample of 299,098 galaxies selected from SDSS DR7 (Abazajian et al. 2009) is shown for comparison. Following Juneau et al. (2014), galaxies were selected to have well-constrained [O III]/H β and [N II]/H α line ratios ($S/N > 3/\sqrt{2}$, corresponding to each line with $S/N > 3$ or to combinations of a weaker and a stronger line, provided that the overall line ratio is constrained to this minimum significance). Line flux measurements and uncertainties were taken from the MPA/JHU catalogs, and adjusted as detailed by Juneau et al. (2014). A systematic shift with respect to the locus of SFGs in the local universe is present, qualitatively in agreement with a possible increase of the hardness of the radiation field, even if the data at our disposal do not allow us to recognize a specific direction of the shift. To exclude AGNs from our sample, we used the conservative line of exclusion as a function of redshift provided by Equation (5) in Kewley et al. (2013a). Alternative emission line diagnostics relying on [O III]/H β and either host color or stellar mass have been developed (e.g., Juneau et al. 2011; Yan et al. 2011). However, $\sim 50\%$ of the field stacked sample (15/31 sources) does not have H β in the observed range. To obviate this issue, we coupled the BPT diagnostics with the [N II]/H α –observed H α equivalent width ($\text{EW}(\text{H}\alpha)$) diagram (Figure 6). The local SDSS sample is shown again for comparison (here we considered only galaxies with $S/N(\text{EW}(\text{H}\alpha))) > 3$, cutting the BPT local sample to 272,562 objects). In this diagram, [N II]/H α traces the ionized

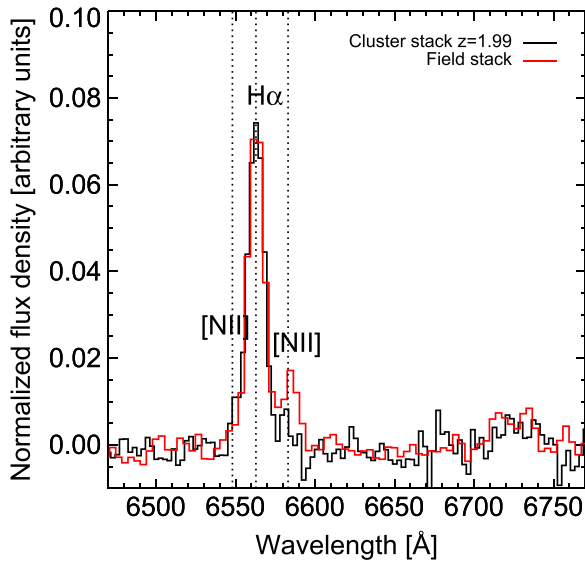


Figure 4. Black and red lines, respectively, represent the continuum-subtracted MOIRCS stacked spectra of the sample of 6 cluster SFGs and 31 field SFGs in the mass range of $10 \leq \log(M/M_\odot) \leq 11$ with $H\alpha$ and $[N II]$ in the observed wavelength range, normalized to $H\alpha$ fluxes. Vertical dotted lines mark the expected location of emission lines of interest, as labeled.

gas conditions, as higher $[N II]/H\alpha$ values are connected to harder powering sources, while $EW(H\alpha)$ measures the power of the ionizing source in relation with the continuum emission of the underlying stellar populations (Cid Fernandes et al. 2010, 2011). In this diagram, all of the potential AGNs that we selected on the BPT basis occupy the same region at high $[N II]/H\alpha$ ratios. In total, we conservatively excluded 22 objects as AGN-powered sources and none of these sources were included in the stacked spectra. Four points above the nominal line of exclusion in the BPT were not discarded as their upper limits on $[N II]/H\alpha$ are still compatible with the star-forming region in the $[N II]/H\alpha$ –observed $EW(H\alpha)$ diagram. We note that 3/4 objects have $\log(M/M_\odot) < 10$ and thus are not part of the stacked spectra. Excluding the fourth BPT potential outlier from the field stacked spectrum would slightly strengthen the significance (well within the uncertainties) of the main results of this work, increasing the $[N II]/H\alpha$ field average value (see below). Even if we cannot exclude potential AGN contamination for these sources, we lack definitive evidence that they are mainly AGN-dominated and, keeping the most conservative approach in terms of significance of the final results, we retained these four objects in the final samples. Among these 22 sources, 2 are known to be a soft and a hard X-ray AGN in CL J1449+0856, both with $\log(M/M_\odot) > 11$ (G13), while 2 other field objects are massive radiogalaxies in the COSMOS field. All of these independently known AGNs lie either above the line of exclusion in the BPT diagram or above $\log([N II]/H\alpha) = -0.4$ in the $[N II]/H\alpha$ –observed $EW(H\alpha)$ plane, as expected. We note here that the choice of the AGNs to remove does not change if we consider a dereddened $EW(H\alpha)$. In Figure 6, we show in addition the position of the cluster and field stacked values. Comparing these two, we note that the cluster and field samples show a $>4\sigma$ significant difference in $[N II]/H\alpha$. Considering the subsample of 16 field galaxies with all the BPT lines, the difference is still tentatively present ($\sim 2.7\sigma$), even if the significance is reduced due to lower number statistics and S/N. Moreover, in this case the

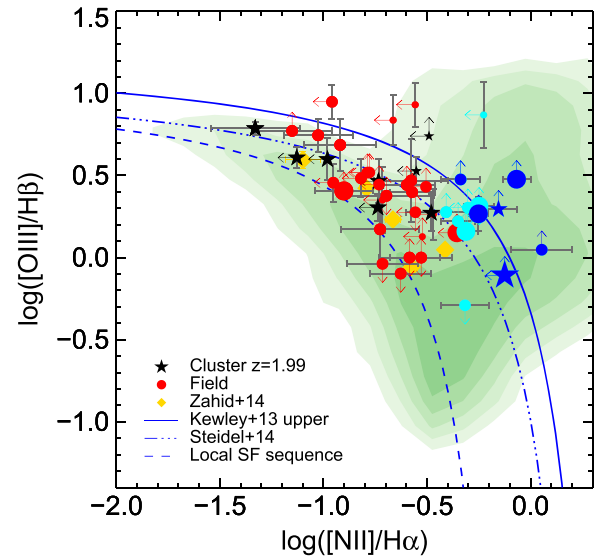


Figure 5. BPT diagram for the MOIRCS spectroscopic sample. Red circles and black stars represent the field and cluster samples, respectively. Cyan and blue symbols mark the objects excluded from the SF sample as AGNs from X-ray, radio, $[N II]/H\alpha$ – $EW(H\alpha)$, or the solid curve shown (see the text and Figure 6 for details). Symbol sizes scale as the stellar mass. Golden diamonds represent the stacked points from the FMOS survey at $z \sim 1.55$ (Zahid et al. 2014b). Arrows indicate 2σ upper and lower limits both for the x and y axes. The blue dashed line shows the local SF sequence (Equation (3), Kewley et al. 2013a), the blue dash-dotted line indicates the empirical SF sequence at $z \sim 2.3$ from Steidel et al. (2014), and the blue solid line is the AGN-SFG dividing line at $z = 2$ (Equation (5), Kewley et al. 2013a). Green shaded contours show the SDSS $z \sim 0.1$ sample.

cluster and field $[O III]/H\beta$ ratios are fully compatible within the error bars (0.585 ± 0.062 and 0.591 ± 0.058 dex, respectively). As a consequence, the $([O III]/H\beta)/([N II]/H\alpha)$ ratio is compatible between the two samples, given the increased uncertainties. Figure 6 shows also a 0.37 dex difference ($\sim 4.7\sigma$ significant) in the observed $EW(H\alpha)$ between the cluster and the field, which reflects the 2.5 times higher observed $H\alpha$ luminosity in the cluster stack (see Section 3.3.4 for further discussion). Finally, we observe a significant $[S II] \lambda\lambda 6716, 6731$ emission in the stacked spectra, but the S/N is not high enough to accurately measure the ratio of the two lines and hence directly estimate the electron density n_e (Osterbrock & Ferland 2006). Therefore, we fixed this ratio compatibly with typical n_e values in $[H II]$ regions ($n_e = 100$ – 1000 cm^{-3} , Osterbrock & Ferland 2006) and measured the total combined flux $[S II]_{\text{tot}} = [S II] \lambda\lambda 6716 + \lambda 6731$ reported in Table 4.

3.3.2. Gas-phase Metallicities

Different methods have been proposed through the years to estimate the gas-phase metallicity in galaxies. The safest method involves the ratio of the $[O III] \lambda 4363$ auroral line and lower excitation lines as $[O III] \lambda\lambda 4959, 5007$, which allows us to directly evaluate the oxygen abundance through the gas electron temperature (T_e). However, $[O III] \lambda 4363$ is weak even in low-metallicity regions and generally difficult to measure in high-redshift galaxies. Other empirical methods have been proposed to circumvent this problem, calibrating the ratios of stronger lines against T_e in $H II$ regions. Alternatively, theoretical photoionization models may be employed to predict the line fluxes and derive the gas-phase abundances (see Kewley & Ellison 2008 for a census of gas-phase metallicity

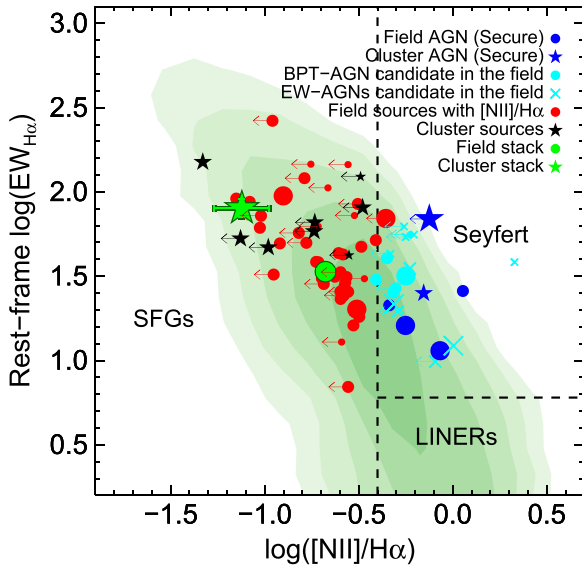


Figure 6. $[\text{N II}]/\text{H}\alpha$ –rest-frame reddening uncorrected $\text{EW}(\text{H}\alpha)$ diagram for the MOIRCS spectroscopic sample. Red circles and black stars represent the field and cluster samples, respectively. Blue circles and stars, respectively, represent field and cluster AGNs known from X-ray, radio, and BPT diagram. Cyan symbols represent AGN candidates in the present diagram and in the BPT. Symbol sizes scale as the stellar mass. Arrows indicate 2σ upper limits. The green circle and star represent the field and cluster stack, respectively. Green shaded contours show the SDSS $z \sim 0.1$ sample.

calibrations). In general, the use of different methods leads to a systematic difference in absolute metallicity values of up to ~ 0.3 dex (Kewley & Ellison 2008). Relative comparisons among different samples from different studies are still meaningful if all the measurements are reported to the same calibration system. For this work, we decided to use the $\text{N2} = \log([\text{N II}]/\text{H}\alpha)$ metallicity indicator, given the presence of both $[\text{N II}]$ and $\text{H}\alpha$ in a relatively clear window of the K_s band at $z = 2$. Pettini & Pagel (2004, PP04 in the following) calibrated N2 against the T_e method in a local sample of H II regions, expressing the gas-phase metallicity as

$$12 + \log(\text{O}/\text{H})_{\text{N2,PP04}} = 0.57 \times \text{N2} + 8.90 \quad (1)$$

with a quoted uncertainty of ~ 0.18 dex. Partial drawbacks of using N2 are its sensitivity to the ionization parameter \mathcal{U} and the saturation of the index at solar metallicities and above, as $[\text{N II}]$ becomes the dominant coolant (Baldwin et al. 1981; Kewley & Dopita 2002). The impact of this saturation does not seem to dramatically affect the final metallicity estimate, resulting in a ~ 0.03 dex underestimate of the final abundance (Zahid et al. 2014a). Other indicators do not suffer from this saturation issue and could potentially be used to confirm the metallicity estimate. When all lines were available, we used the $\text{O3N2} = \log([[\text{O III}]/\text{H}\beta]/([\text{N II}]/\text{H}\alpha])$ as an alternative metallicity indicator. In this case, the PP04 calibration gives

$$12 + \log(\text{O}/\text{H})_{\text{O3N2,PP04}} = -0.32 \times \text{O3N2} + 8.73 \quad (2)$$

with a quoted uncertainty of ~ 0.14 dex. The inclusion of $[\text{O III}]$ in the ratio should guarantee sensitivity to increasing metallicity even above solar, as $[\text{O III}]$ continues to decrease while $[\text{N II}]$ saturates. In practice, we could estimate this index at 3σ confidence only for very few individual sources and for the stacked spectra (Figure 7). In the local universe, these two indicators provide consistent metallicity estimates (Kewley &

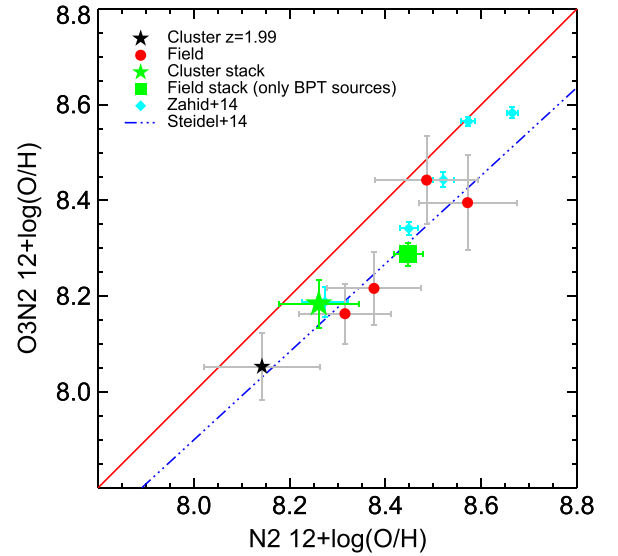


Figure 7. Gas-phase metallicities derived using the N2 and O3N2 indicators calibrated by Pettini & Pagel (2004). Red circles and black stars, respectively, mark individual field and cluster 3σ detections of each line in the O3N2 indicator. The green filled square and star, respectively, represent the measurement for the subsample of 16 field SFGs and cluster stacked sample in the $10 \leq \log(M/M_\odot) \leq 11$ range. Cyan circles mark the stacked values at $z \sim 1.55$ from (Zahid et al. 2014b). The blue dashed-dotted line is the linear relation between N2 and O3N2 for the $z \sim 2.3$ from Steidel et al. (2014). A one-to-one red line is shown as a comparison.

Ellison 2008). On the contrary, for our samples of high- z galaxies the N2 indicator returns systematically higher gas-phase metallicities compared to the O3N2 indicator (Figure 7), in agreement with other recent findings (Erb et al. 2006; Yabe et al. 2012; Zahid et al. 2014b; S14). Different interpretations and prescriptions to avoid systematic errors have been proposed in several studies (i.e., S14), even if all of them remain quite speculative in the absence of a direct $12 + \log(\text{O}/\text{H})$ measurement, i.e., by means of the T_e method. However, all of the studies agree on a probable overall change of the ISM conditions in high- z galaxies with respect to the local universe, as indicated by independent observations (Magdis et al. 2012; Kashino et al. 2013). In principle, an evolution in the hardness of the radiation field, electron density, ionization parameter, or nitrogen-to-oxygen ratio can make the calibration intrinsically wrong for high-redshift galaxies. In their recent work, S14 recalibrated the N2 indicator on a sample of local H II regions matching the physical conditions of their $z \sim 2.3$ galaxies, obtaining

$$12 + \log(\text{O}/\text{H})_{\text{N2,S14}} = 0.36 \times \text{N2} + 8.62 \quad (3)$$

with a quoted total scatter of ~ 0.13 dex. S14 found that N2 is less sensitive to metallicity variations than implied by the PP04 calibration, which substantially overpredicts the metallicities at high redshifts. On the contrary, after S14 recalibration, the O3N2 indicator predicts metallicities similar to those given by the PP04 calibration, especially with the inclusion of a term depending on N/O (Pérez-Montero & Contini 2009):

$$12 + \log(\text{O}/\text{H})_{\text{O3N2,S14}} = -0.28 \times \text{O3N2} + 8.66 \quad (4)$$

with a total uncertainty of ~ 0.12 dex. Reducing the sensitivity of the N2 calibrator to the gas-phase metallicity and leaving intact the one of O3N2, the two ratios predict consistent abundances at $z \sim 2$.

Table 5
Gas-phase Metallicity Estimates for the Stacked Spectra

Environment	$\log(M)$	$12 + \log(\text{O}/\text{H})^a$			
		N2		O3N2	
	$\log(M_\odot)$	PP04 ^b	S14 ^c	PP04 ^b	S14 ^c
Cluster	10.47	8.261 ± 0.083	8.216 ± 0.053	8.184 ± 0.051	8.182 ± 0.044
Field	10.57	8.514 ± 0.025	8.376 ± 0.016	8.287 ± 0.025^d	8.273 ± 0.022^d

^a For comparison, the solar value is $12 + \log(\text{O}/\text{H}) = 8.69$ (Asplund et al. 2009).

^b Pettini & Pagel (2004) calibration.

^c Steidel et al. (2014) calibration.

^d Values for the subsample of 16 field SFGs with $\text{H}\beta$ and $[\text{O III}]$ in the observed wavelength range.

As mentioned, a cause of concern when estimating gas-phase oxygen abundance through indirect indicators involving other species as N2 and O3N2 is the abundance of these elements relative to oxygen. In the case of N2 and O3N2 indicators, an assumption on the N/O ratio is implied in every calibration, explicitly or implicitly, and ignoring the N/O ratio could result in a systematic effect in the O/H estimation (Pérez-Montero & Contini 2009). An estimation of N/O can be derived from the $\text{N2O2} = \log([\text{N II}]/[\text{O II}])$ ratio, as calibrated in the local universe by Pérez-Montero & Contini (2009):

$$\log(\text{N/O}) = 0.93 \times \text{N2O2} - 0.20 \quad (5)$$

with a standard deviation of the residuals of 0.24 dex. We could estimate N/O for the cluster stacked sample thanks to the WFC3 $[\text{O II}]$ determination after proper dust reddening correction (see next section). This was not possible for the field sample, preventing a fully consistent environmental comparison of N/O. In our case, the inclusion of a N/O correction term in the PP04 N2 calibration (Equation (13) from Pérez-Montero & Contini 2009) leaves virtually unchanged the metallicity estimate for the cluster ($a \sim 0.05$ dex difference, well within the calibration errors). The observed cluster N/O ratio ($\log(\text{N/O}) = -1.18 \pm 0.15$) is lower than the solar value ($\log(\text{N/O}) \simeq -0.86$, Pilyugin et al. 2012), and close to the “primary” nitrogen abundance predicted by current models ($\log(\text{N/O}) \simeq -1.5$, Charlot & Longhetti 2001; Pilyugin et al. 2012; Pérez-Montero & Contini 2009; Andrews & Martini 2013; Dopita et al. 2013) in agreement with the estimated low gas-phase metallicity value. Interestingly, recent works on samples at redshift $z \sim 2$ found a N/O ratio consistent with the solar value and only slowly or not varying with the O/H ratio, and hence with the gas-phase metallicity, at least for highly star-forming systems typical at these redshifts ($\text{SFR} \geq 10 M_\odot \text{yr}^{-1}$, Andrews & Martini 2013, S14). An alternative explanation is that $z \sim 2$ SFGs show higher N/O ratios at fixed metallicities than local counterparts at low masses ($M \lesssim 10^{10.11} M_\odot$ in Shapley et al. 2014, and $M \sim 10^9 M_\odot$ Masters et al. 2014). If we consider N/O ratios from literature as representative of a general field sample (but check Kulas et al. 2013 for the study of protocluster members in S14 sample) in a mass range and excitation conditions similar to those of our cluster sample, they result to be ~ 0.2 dex higher than the value measured on the cluster stacked spectrum.

Further indications of the lower metal content in cluster sources are the lower $[\text{N II}]/[\text{S II}]_{\text{tot}}$ and higher $(\text{H}\alpha + [\text{N II}])/[\text{S II}]_{\text{tot}}$ ratios than the field counterparts (Nagao et al. 2006), even if affected by substantial uncertainties. Moreover, for the

cluster stacked sample we estimated the ionization parameter and the gas-phase metallicity using the iterative method of Kobulnicky & Kewley (2004), which involves the $R_{23} = ([\text{O II}]\lambda 3727 + [\text{O III}]\lambda\lambda 4959, 5007)/\text{H}\beta$ and $O_{32} = [\text{O III}]\lambda\lambda 4959, 5007/[\text{O II}]\lambda 3727$ indicators. $\text{H}\beta$, and $[\text{O III}]$ fluxes. After applying the Kewley & Ellison (2008) conversion to PP04 N2 metallicities, we obtain $12 + \log(\text{O}/\text{H}) = 8.217$ with ~ 0.15 dex accuracy, thus compatible with our estimate based on $[\text{N II}]/\text{H}\alpha$ (Table 5). We also obtained a ionization parameter $U \simeq -2.61$, which is comparable to values measured in high-redshift galaxies ($-2.9 < U < -2.0$, Kewley et al. 2013a, and references therein). Hence a high-ionization parameter may not be the main driver of the $[\text{N II}]/\text{H}\alpha$ difference that we observed between cluster and field, even if we cannot completely exclude possible effects connected to U in our analysis.

Overall, while various metallicity estimators may differ on an absolute scale, the systematic difference found between the cluster and the field is robust. Given the lower number of sources with safe O3N2 measurements, we privileged N2 as the primary metallicity indicator. All the gas-phase metallicity estimates are reported in Table 5: in the same mass range, the cluster sample results 0.09–0.25 dex (using O3N2_{S14} and N2_{PP04}, respectively) more metal-poor than the field sample, depending on the calibration used.

3.3.3. Nebular $E(B-V)$ Estimate

The dust reddening on stellar light ($E(B-V)_{\text{cont}}$) was estimated through SED fitting. However, the amount of dust attenuation toward the emission lines ($E(B-V)_{\text{neb}}$) is typically larger than $E(B-V)_{\text{cont}}$. Calzetti et al. (2000) find a factor $f = E(B-V)_{\text{cont}}/E(B-V)_{\text{neb}} = 0.44$ between the two color excesses in the local universe, adopting the Fitzpatrick (1999) law for the nebular reddening and their own law for the continuum reddening ($f = 0.52$ using the Calzetti et al. 2000 reddening law for both the nebular emissions and the continuum). Recent works suggest that this continuum-to-nebular emission differential reddening factor is generally higher for high-redshift galaxies, reducing the difference between stellar and nebular continuum (Kashino et al. 2013; Pannella et al. 2014). Here we attempt to estimate this factor using the Balmer decrement $\text{H}\alpha/\text{H}\beta$ and assuming a Case B recombination with a gas temperature of $T = 10^4$ K and an electron density $n_e = 100 \text{ cm}^{-3}$, according to which the intrinsic ratio $\text{H}\alpha/\text{H}\beta$ is equal to 2.86 (Osterbrock & Ferland 2006). From the observed $\text{H}\alpha$ and $\text{H}\beta$ values it is

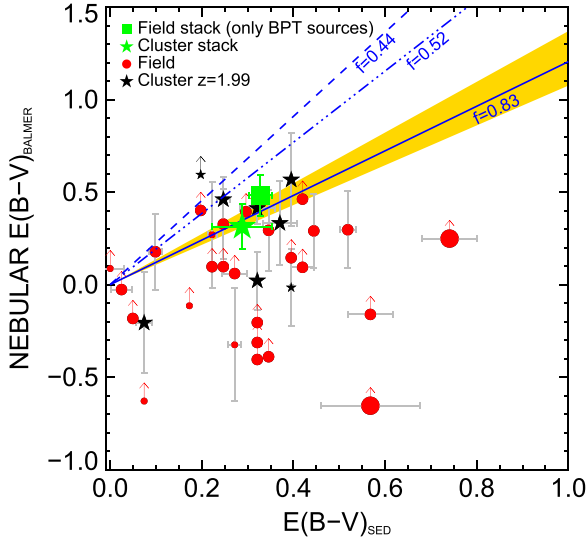


Figure 8. Reddening estimates based on SED fitting and Balmer decrement. Red circles and black stars, respectively, mark field and cluster SFGs with 3σ $H\alpha$ and $H\beta$ detections. Symbol sizes scale as stellar mass. Arrows mark 3σ lower limits. The green square and star indicate the subsample of 16 field sources with measured $[O\text{ III}]$ and $H\beta$ and the cluster stacked values, respectively. The blue dashed and dotted-dashed lines represent the $f = 0.44$ ($f = 0.52$) ratio $E(B-V)_{\text{cont}}/E(B-V)_{\text{neb}}$ obtained in the local universe applying Fitzpatrick–Calzetti (Calzetti–Calzetti) laws for the nebular and continuum reddening, respectively. The blue solid line and the shaded area represent the same ratio using a Calzetti law for both the nebular and continuum reddening and the relative uncertainties quoted in Kashino et al. (2013) for the sample of $z \sim 1.55$ galaxies from the FMOS survey, where $f = 0.83$.

possible to compute

$$E(B-V)_{\text{neb}} = \frac{2.5}{k_{H\beta} - k_{H\alpha}} \log \left[\frac{H\alpha/H\beta}{2.86} \right] \quad (6)$$

assuming a proper extinction law. In this work, we assumed the Calzetti et al. (2000) law for both the nebular and continuum reddening, for which $k_{H\beta} = 4.598$ and $k_{H\alpha} = 3.325$.

A limited sample of galaxies with a safe 3σ $H\beta$ detection is available to measure the Balmer decrement on an object-by-object basis. However, we used the values from the stacked spectra to assess this issue for the mean population of SFGs in our sample. In Figure 8, we show the relation between SED based $E(B-V)_{\text{cont}}$ and $E(B-V)_{\text{neb}}$ derived from the Balmer decrement. The best fitting slope for the 3σ detected stacked values is 0.74 ± 0.22 , consistent within the uncertainties with the results from the FMOS survey at $z \sim 1.55$ (Kashino et al. 2013), but still formally in agreement with the local value obtained using the same reddening law. Our best-fit value is in agreement with the alternative estimate that we derived from the fitting of the $E(B-V)_{\text{cont}}\text{-SFR}_{H\alpha}^{\text{uncorr}}/\text{SFR}_{UV}^{\text{uncorr}}$ relation as in Figure 3 of Kashino et al. (2013), namely $f = 0.74 \pm 0.05$.

We checked for possible environmental signatures in the stellar mass–reddening relation (MRR), comparing the cluster and field samples. Figure 9 shows the MRR for our sample of cluster and field SFGs. Both the stellar mass and the reddening estimates come from the SED fitting procedure. In Figure 9, both the cluster and field samples follow the same trend, not revealing any environmental signature in the MRR. Applying a simple linear regression separately for the two samples, we obtain compatible slopes: 0.78 ± 0.42 and 0.59 ± 0.07 for the cluster and field sample, respectively.

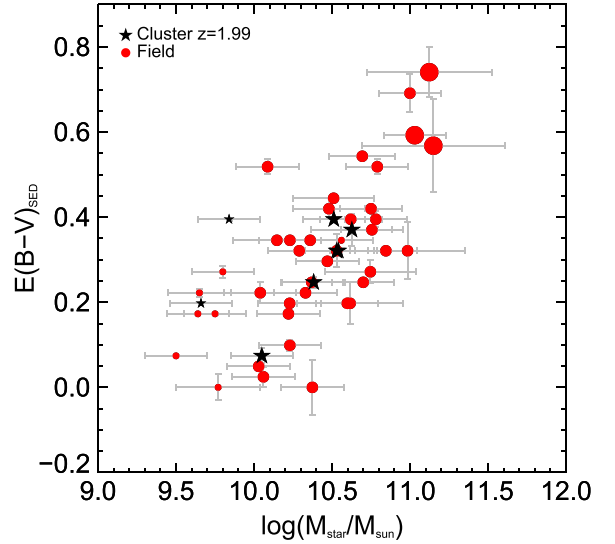


Figure 9. Mass–reddening relation for the MOIRCS spectroscopic sample of SFGs. Red circles and black stars mark the field and cluster samples, respectively. Symbol sizes scale as the stellar mass.

3.3.4. A Significant Difference in the Observed $EW(H\alpha)$

As shown in Figure 6, there is a 0.37 dex difference ($\sim 4.7\sigma$ significant) in the observed $EW(H\alpha)$ between the cluster and the field. Such a difference may arise from an enhanced specific star formation rate (sSFR), a variation in the dust reddening correction $E(B-V)$, or in the continuum-to-nebular emission differential reddening factor f between cluster and field, as $EW(H\alpha) \propto \text{sSFR} \times 10^{0.4E(B-V)_{\text{cont}}} k_{H\alpha}(1/f-1)$. Assuming a common f value in cluster and field SFGs and the average $E(B-V)_{\text{cont}}$ values in Table 3, the difference in the observed $EW(H\alpha)$ is translated into a significant difference in intrinsic $EW(H\alpha)$ and ascribable to enhanced sSFR in cluster sources. As f is physically linked to the average geometric dust distribution in galaxies star-forming regions (Kashino et al. 2013), there are no immediately evident reasons why the environment should play a role in setting this factor. Hence, considering f constant within different environments would not be a strong assumption. However, we could let this parameter free as well, resulting in a more conservative approach: in this case, the f factor for the field stack is tentatively lower than for the cluster sample, reducing the difference in intrinsic $EW(H\alpha)$. Moreover, individual estimates of f are hampered by large error bars on the Balmer decrement measurements (Figure 8), not allowing to fully decouple sSFR and reddening effects. Since the two stacked samples have similar stellar masses, an enhancement in sSFR would reflect the 2.5 times higher $H\alpha$ observed luminosity in the cluster stack (Tables 3–4). However, when converting $H\alpha$ fluxes to SFR applying the Kennicutt (1998) conversion and the reddening correction, the values for cluster and field are formally compatible. In Figure 10, we show the field and cluster sources in the final stacked samples in the stellar mass– $\text{SFR}_{H\alpha}$, SFR_{SED} plane. All the SFRs have been rescaled by a factor of $[(1+z)/(1+1.99)]^{2.8}$ to match the cluster redshift. We adopted the MS parametrization given in Sargent et al. (2014) as a reference. In the right panel, individual cluster sources seem tentatively more star-forming than the field counterparts, populating the upper envelope of the MS, and the lowest $[N\text{ II}]/H\alpha$ ratio corresponds to the highest $\text{SFR}_{H\alpha}$. However, the average properties of the

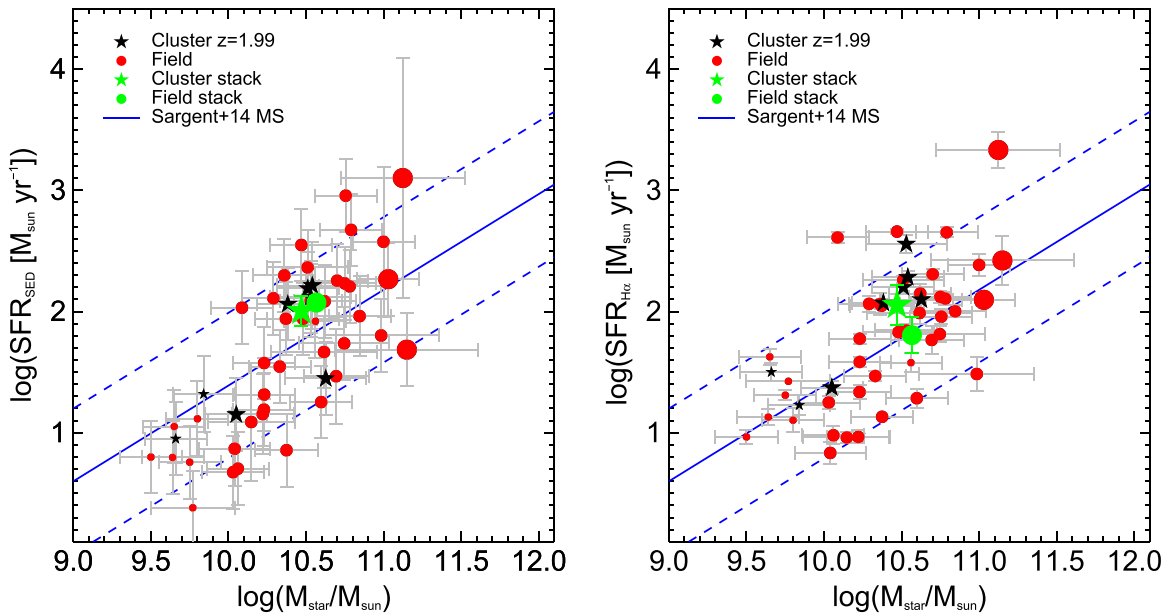


Figure 10. Stellar mass vs. SFR. Red circles and black stars mark the field and cluster SFGs, respectively. Symbol sizes scale as the stellar mass. The green circle and star indicate the field and cluster stacked values, respectively. The blue solid line indicates the MS at $z = 2$ as parametrized in Sargent et al. (2014). The blue dashed lines mark the ± 0.6 dex scatter. Left panel: $H\alpha$ derived SFR. Right panel: SED derived SFR.

cluster and field populations in the same mass regime are formally compatible, as shown by the stacked values, and this is likely due to the uncertainties on individual f factor estimates. The stacked values are also compatible when considering SFR_{SED} , as shown in left panel of Figure 10, but this may be partly due to the longer timescales probed by the UV stellar emission as a SFR indicator with respect to $H\alpha$ ($t_{UV} \sim 100$ Myr, $t_{H\alpha} \sim 10$ Myr), which makes SFR_{SED} insensitive to potentially recent episodes of star formation in cluster sources with respect to the field. For reference, we show the comparison between SED- and $H\alpha$ -based SFRs in Figure 11, where SFR_{SED} for the stacked samples is the mean of the single sources values.

In the most conservative approach, considering the uncertainties on the f factor, we cannot fully disentangle the reddening and sSFR (or SFR) effects in producing the observed $EW(H\alpha)$ difference. However, reasonably assuming the f factor as independent of the environment and the average $E(B - V)_{cont}$ values from SED modeling, we can decouple the two effects, ascribing the enhanced observed $EW(H\alpha)$ in cluster sources to an enhancement in sSFR. In any case, we emphasize how Figure 6 shows another significant difference between cluster and field SFGs resulting from this work, in addition to the lower gas-phase metallicity.

4. THE MASS-METALLICITY RELATION

The presence of a correlation between stellar mass and metallicity in SFGs has been known for a long time (Lequeux et al. 1979), both locally (Tremonti et al. 2004) and at increasing redshift (Erb et al. 2006; Kewley & Ellison 2008; Zahid et al. 2012, 2014a; Cullen et al. 2014; Steidel et al. 2014; Wuyts et al. 2014, and many others). This relation can be interpreted as the result of the interplay among the accretion of metal-poor pristine gas, star formation episodes, and enriched gas expulsion through stellar winds (Davé et al. 2012; Lilly et al. 2013; Zahid et al. 2014a). At higher redshifts the overall observed metallicity is lower than in local galaxies, virtually

shifting the observed MZR vertically with redshift. In Figure 12, we show the observed $[N II]/H\alpha$ ratio, a proxy for gas-phase metallicity, as a function of stellar mass. A $>4\sigma$ significant lower ratio is observed in the cluster stack with respect to the field mass-matched sample. This result is unchanged if we consider as a field $[N II]/H\alpha$ representative value the linear interpolation at $z = 1.99$ of the $z \sim 1.55$ and $z \sim 2.3$ values from Zahid et al. (2014b) and S14, at fixed mass. Quantitatively, the metallicity difference between the cluster and field samples depends on the adopted calibration for $[N II]/H\alpha$ as shown in the left panels of Figure 13. In the same figure, we show the metallicity derived from the O3N2 indicator (right panels) for the subsample of 16 intermediate mass field SFGs with $H\beta$ and $[O III]$ measurements. Also in this case, given the comparable $[O III]/H\beta$ values of the cluster and the field samples, the difference in the final metallicity values reflects the different $[N II]/H\alpha$ ratio through the slope of the adopted linear O3N2 calibration—i.e., through the sensitivity to metallicity variations assigned to $[N II]/H\alpha$. Metallicity differences vary between 0.09 and 0.25 dex from O3N2_{S14} and N2_{pp04} calibrations, respectively. Given the low number statistics, we do not attempt any fit to the observed points in Figure 12, neither stacked nor single.

Recently, the possible introduction of a third term in the MZR has been advocated to reduce the intrinsic scatter of the relation. Mannucci et al. (2010) proposed to add the SFR to build the so-called “Fundamental Mass-Metallicity Relation” (FMR) and provided a suitable description of it through the $\mu_\alpha = \log(M/M_\odot) - \alpha \log(SFR/M_\odot \text{ yr}^{-1})$ parameter. They found that the minimum scatter for their local sample from the SDSS is reached for $\alpha = 0.32$, and that this value does not evolve at least up to $z \sim 2.5$. This latter finding is somewhat in contrast with recent works at $z \gtrsim 1.5$ (Wuyts et al. 2014; Zahid et al. 2014a, 2014b; S14) and, partially, with the results of the present study (but see Maier et al. 2014 for the impact of the choice of the FMR extrapolation on the evolution with z). Figure 14 shows the FMR projection on the $\mu_{0.32-12} + \log(O/H)$

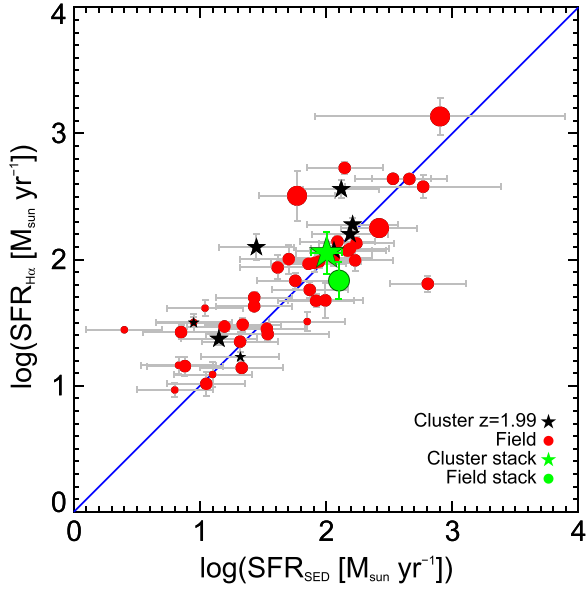


Figure 11. SFR estimates from SED fitting and intrinsic $H\alpha$ luminosities for the MOIRCS spectroscopic sample of SFGs. Red circles and black stars, respectively, mark the field and cluster samples with 2σ detected $H\alpha$ line. Symbol sizes scale as the stellar mass. The green circle indicates the field stacked value. The green star indicates the cluster stacked value. A one-to-one blue line is shown as a comparison.

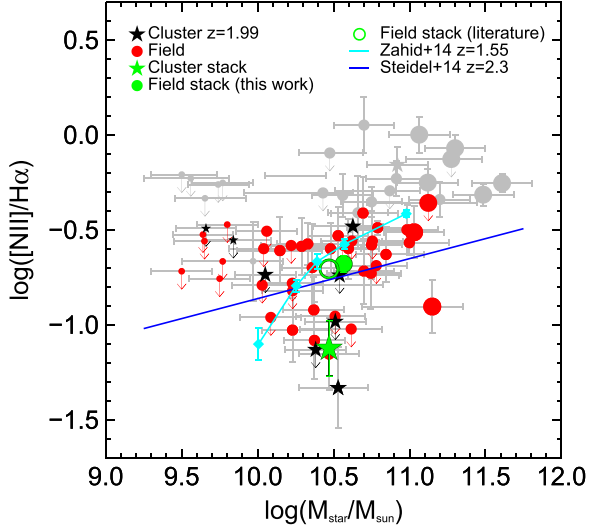


Figure 12. Mass- $[N II]/H\alpha$ relation for the MOIRCS spectroscopic sample. Red circles and black stars represent the field and cluster samples, respectively. Gray symbols mark the objects excluded from the SF sample as AGNs (see Section 3.3.1). Arrows indicate 2σ upper limits. Symbol sizes scale as the stellar mass. The green solid circle and star represent the field and cluster stacked samples, respectively. The green empty circle marks the expected field position at $z = 2$ from the interpolation of literature data (see the text for details). Cyan diamonds represent the stacked points from the FMOS survey at $z \sim 1.55$ (Zahid et al. 2014b). The blue solid line is the relation for the $z \sim 2.3$ sample from Steidel et al. (2014, Equation (20)).

plane as parametrized in Equation (4) of Mannucci et al. (2010), where we used $SFR_{H\alpha}$. Again, the choice of the indicator (and especially of its calibration) is decisive for the absolute value of the metallicity, which enters the FMR. In Figure 14, we show the PP04 N2 calibration, which, in the case of the field sample, is consistent with the FMR trend, after a

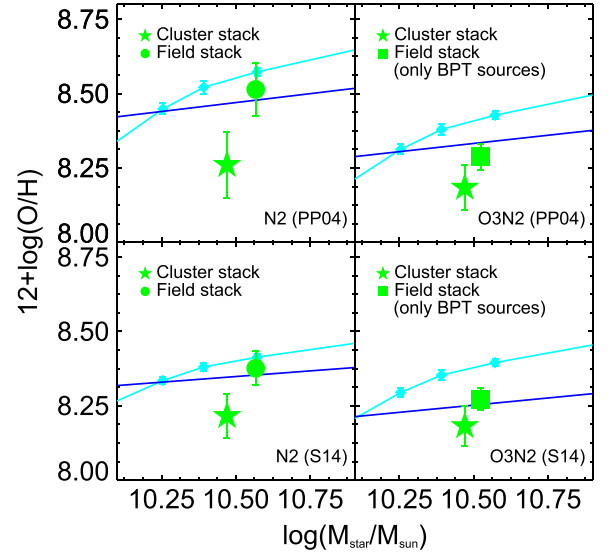


Figure 13. MZR for the MOIRCS spectroscopic stacked samples in the mass range $10 \leq \log(M/M_\odot) \leq 11$. The green circle and square indicate the 31-source and 16-source field stacked values, respectively. The green star indicates the cluster stacked value. Cyan diamonds represent the stacked points from the FMOS survey at $z \sim 1.55$ (Zahid et al. 2014b) and the blue solid line is the relation for the $z \sim 2.3$ sample from Steidel et al. (2014, Equation (17)), both rescaled to match the metallicity calibration in each panel (see the legend).

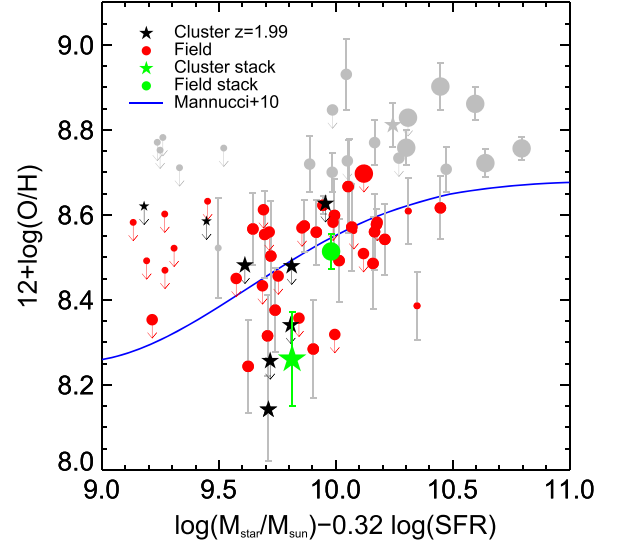


Figure 14. FMR for the MOIRCS spectroscopic sample. Red circles and black stars represent the field and cluster samples, respectively. Gray symbols mark the objects excluded from the SF sample as AGNs (see Section 3.3.1). Arrows indicate 2σ upper limits. Symbol sizes scale as the stellar mass. The green solid circle and star represent the field and cluster stacked samples, respectively. SFRs are estimated from $H\alpha$ fluxes (see Section 3.3.4 for details). The gas-phase metallicity is estimated from the N2 indicator as calibrated by Pettini & Pagel (2004). The blue solid line represents the polynomial parametrization of the FMR by (Mannucci et al. 2010, Equation (4)).

proper conversion from the Maiolino et al. (2008) calibration system to PP04. In the same figure, the cluster value is tentatively inconsistent ($\sim 2.7\sigma$) with an unevolving FMR up to $z \sim 2.5$. After proper metallicity rescaling, we observe a similar inconsistency with the prediction of the analytically derived $Z(M, SFR)$ by Lilly et al. (2013; left panel of their Figure 7).

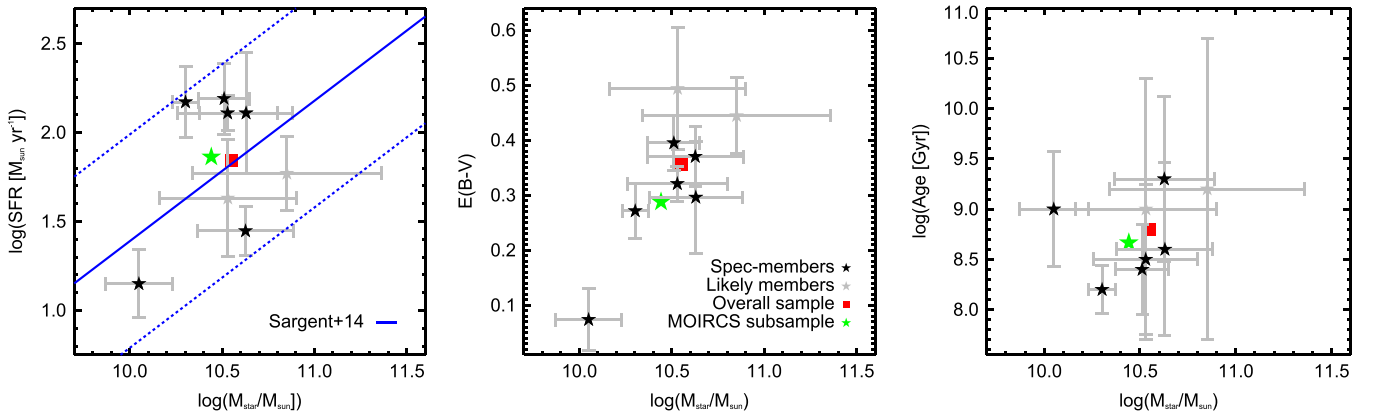


Figure 15. Photometric properties of the cluster “parent” sample from which the high priority sample for MOIRCS follow-up has been extracted. In each panel, black stars mark the six WFC3 spectroscopically confirmed SF cluster members in the $10 \leq \log(M/M_\odot) \leq 11$ mass range, which have been followed-up with MOIRCS and stacked. Gray stars mark the candidate members in the same mass range not observed with MOIRCS. The green star and red square indicate the mean value for the sample of followed-up sources and for the overall population, respectively. Left panel: stellar mass vs. SED-based SFR. The MS at $z = 2$ is represented with a ± 0.6 dex scatter as parametrized by Sargent et al. (2014). Central panel: mass–reddening relation. Right panel: mass–luminosity-weighted age relation for constant SFH.

5. DISCUSSION

5.1. Potential Selection Effects

We checked for possible biases in our field sample comparing it to trends from other surveys at similar redshifts and extrapolating them to $z = 1.99$ (Section 4). As shown in Figure 12, our selection of field sources gives results that are consistent with much broader samples in the literature (Zahid et al. 2014b, S14). This shows that our selection is not biased toward specific high-redshift galaxy populations, but extracts a representative sample of MS-SFGs at $z \sim 2$. This result is confirmed stacking only *sBZK*-, $H\alpha$ -selected galaxies from the COSMOS mask and comparing them to the general field sample, as we recover fully consistent line ratios (within 1σ uncertainties).

Moreover, for the higher priority assigned to the WFC3-confirmed cluster members over candidates, another possible selection bias could have occurred in the cluster sample. In particular, even if not specifically $[O III]$ -selected, 5/6 SF cluster members in the final stack have an $[O III]$ detection from WFC3, which could have introduced a bias toward the metal poorer cluster members. To check this possibility we investigated the properties of the whole “parent” pool of spectroscopically confirmed and candidate star-forming members in the mass range $10 \leq \log(M/M_\odot) \leq 11$ from which we chose the high priority sample to observe. The mass cut, the constraints on the quality of photometric data, and the SF classification reduced the original pool to eight members in the investigated mass bin. 6/8 are the WFC3 spectroscopically confirmed members that we observed with MOIRCS and which were stacked. The other two sources are candidate members that were not inserted in the final MOIRCS mask because of geometrical constraints in slit positioning. The photometric properties of these eight galaxies are shown in Figure 15. Furthermore, we investigated the reasons for the WFC3 non-detection of the two candidate members, checking whether or not the absence of $[O III]$ detection could have been due to high metallicities, which could have potentially influenced our subsequent analysis of the cluster metal content. From the SED-based SFR and $E(B-V)$ estimates and assuming an intrinsic $H\alpha/H\beta$ ratio equal to 2.86, we derived the expected $H\beta$ observed flux. In both cases, it fell well below the WFC3 3σ detection threshold

(2×10^{-17} erg cm $^{-2}$ s $^{-1}$, G13), showing that these two sources are intrinsically faint rather than metal-rich (if the latter was the case, we should have detected them in $H\beta$ but not in $[O III]$). Moreover, assuming the WFC3 detection threshold, the predicted $H\beta$ flux, and an empirical track describing the observed population at $z = 2$ in the BPT diagram, we estimated the $[N II]/H\alpha$ ratio for these two sources and the metallicity with N2, confirming their homogeneity with the sample of the six galaxies that we stacked. This result does not change using tracks describing only cluster sources, the whole sample of $z \sim 2$ galaxies, or a trend from the literature. We thus conclude that the intrinsic faintness combined with potentially high orders of contamination in the slitless spectroscopy did not allow a detection and a redshift estimate with WFC3. In the Appendix, we show the WFC3 G141 spectra for these two sources. In addition, we could exclude significant biases introduced by low number statistics for the cluster sample (Section 3.2). Therefore, we can be reasonably confident that evident selection effects are not invalidating the analysis presented in this work.

5.2. The Environmental Effect

5.2.1. Comparison with Other Works

The debate about the environmental signatures in the chemical enrichment of cluster galaxies is still ongoing, even in the local universe. The situation for high-redshift clusters is almost unexplored up to date. Kulas et al. (2013) studied the MZR for a sample of 23 SFGs belonging to a $z = 2.3$ protocluster (Steidel et al. 2005). They find a 0.15 dex metallicity enhancement for galaxies inside the overdensity with respect to field counterparts at low masses ($\log(M/M_\odot) \lesssim 10.1$, Chabrier IMF), but no difference at higher masses. Similarly, Shimakawa et al. (2015) find higher gas-phase metallicities in protocluster members than in the field at $z = 2.1$ – 2.5 below $10^{11} M_\odot$. These results are in contrast with the main finding of this work. Unfortunately, we cannot study possible mass trends, given the low number of SFGs in CL J1449+0856 and the high-mass limit for completeness. Moreover the mass range that we explored is somewhere in between the mass bins defined in Kulas et al. (2013), increasing the difficulty of a

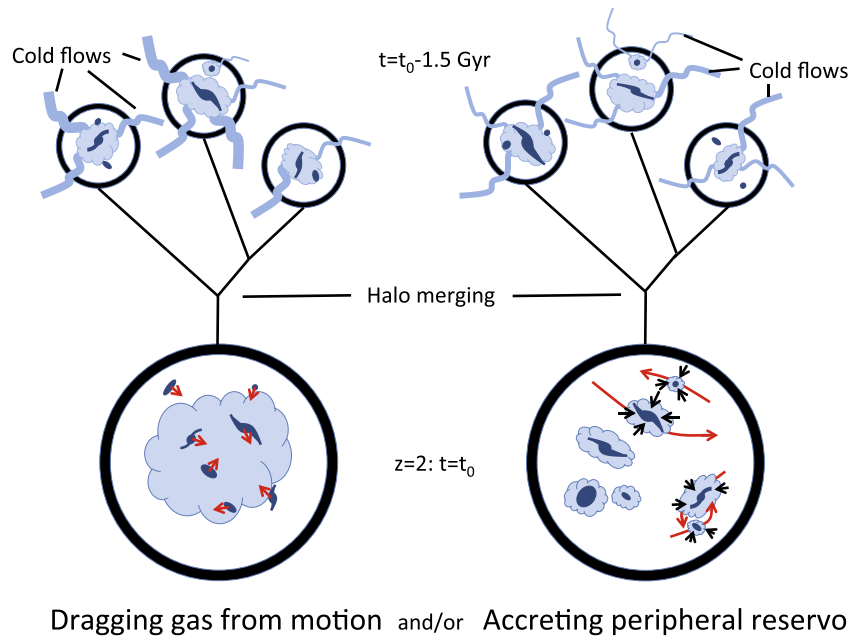


Figure 16. Sketch of the speculative model of gas accretion for SFGs residing in CL J1449+0856. The left branch refers to the possible creation of a gas rich environment in clusters close to a phase of major assembly. The right branch shows the impact of galaxy encounters on the gas halos around each galaxy. The vertical direction marks the time: at the top a phase of gas enrichment occurs ~ 1.5 Gyr before a major phase of assembly of CL J1449+0856 at $z \geq 2$.

direct comparison. Furthermore, we note that contamination from AGNs is a potential issue in selecting SFGs at high redshift: the inclusion of type-2 AGNs, which could be hosted in a non-negligible fraction of high-mass galaxies at $z > 1$ (e.g., Trump et al. 2013), can bias the $[\text{N II}]/\text{H}\alpha$ ratio toward higher values and hence their gas-phase metallicities derived from $N2$. Kulas et al. (2013) selected sources according to UV emission, which should prevent strong AGN contamination (see Steidel et al. 2014). Shimakawa et al. (2015) rejected AGNs using a slight modification of the BPT diagram relying on $\text{H}\alpha$ fluxes and reddening correction to estimate $\text{H}\beta$ fluxes. In this work, we coupled the BPT and $[\text{N II}]/\text{H}\alpha\text{--EW}(\text{H}\alpha)$ diagrams, including X-ray and radio criterion and these different AGN exclusion criteria could have impacted the final results. Furthermore, despite being at comparable redshifts, these overdensities and CL J1449+0856 are structurally different. A pondered definition of *protoclusters* and *clusters* is beyond the scope of this work, but we remark that these different structures may potentially give rise to different effects on their host galaxies, and thus straight comparisons should be made with caution.

5.2.2. The Past History of CL J1449+0856: a Recent Transitional Phase of Stellar Mass Assembly?

The observations presented in this paper have highlighted the presence of a $> 4\sigma$ significant difference in $[\text{N II}]/\text{H}\alpha$ ratio between a sample of SFGs belonging to CL J1449+0856 and a mass-matched sample in the field. This difference is directly translated in a metallicity difference with all the indicators employed in the analysis, so that cluster sources are a factor of 0.09–0.25 dex (using O3N2_{S14} and N2_{PP04} , respectively) more metal-poor than the field counterparts. What follows is a speculation about the origin of this effect. As discussed above, CL J1449+0856 is partially virialized, but a relatively recent phase of assembly must have occurred. According to the model of halo mass growth by Fakhouri et al. (2010), a halo of

$5 \times 10^{13} M_{\odot}$, such as the one hosting CL J1449+0856 (from X-ray emission, G13), should have increased its mass of a factor of times two (times five) in the previous ~ 1 Gyr (~ 1.5 Gyr) of its lifetime. The recent coalescence of multiple less-massive halos could have impacted the hosted galaxies in a twofold way, which is graphically sketched in Figure 16. First, the single bricks forming the final halo could have been gas enriched through cold streams and subsequently merged, thus creating an environment rich in pristine gas. The accretion of cold gas, even in quite massive halos at redshifts close to the formation epoch of CL J1449+0856 progenitors, is consistent with model predictions, if high density, steady, cold streams penetrating the shock heated medium are considered (Birnbom & Dekel 2003; Kereš et al. 2005; Brooks et al. 2009; Dekel et al. 2009a, 2009b). In Figure 17, the mass growth track for CL J1449+0856 halo (Fakhouri et al. 2010) crosses the line separating the hot ISM and cold streams in hot ISM regimes ~ 1 Gyr before $z = 2$ and thus the progenitors of the cluster halo could have been recently enriched with cold gas, before merging. If this gas is not prevented from cooling (Fabian 1994; Revaz et al. 2008; Salomé et al. 2011), given the high dark matter density in $z \gtrsim 2$ halos, it might be dragged and accreted on the galaxies simply moving across it, diluting the metal content. This first effect might not be effective at lower redshifts, where the gas reservoirs in halos are at lower densities, prevented from cooling after the cluster full virialization, chemically enriched by gigayears of stellar formation, and not replenished by cosmological inflows. This latter aspect is illustrated in Figure 17, where the mass growth tracks for a halo of $5 \times 10^{13} M_{\odot}$ at $z = 0, 1$ do not enter the region of cold streams in hot media on timescales of the order of ~ 1 Gyr. Moreover, in a ΛCDM universe, the baryon growth rate scales as $(1+z)^{2.25}$ at fixed mass (Neistein & Dekel 2008). Thus, at low redshifts the progenitors of a halo of such mass cannot be easily refurnished with cold gas.

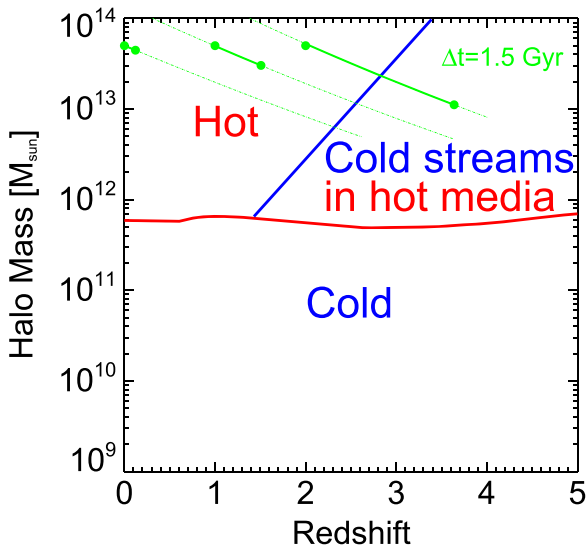


Figure 17. Analytic prediction of the “hot,” “cold,” and “cold streams in hot media” regimes in the mass-redshift space from Dekel et al. (2009b). The green tracks show the mass growth for halos of $5 \times 10^{13} M_{\odot}$ at $z = 0, 1, 2$ (Fakhouri et al. 2010). The solid segments represent a lookback time interval of 1.5 Gyr starting from the redshift of reference.

Second, a recent epoch of the high merging rate of dark matter halos could have favored encounters, fly-bys, and mergers among the galaxies hosted in the merging halos, given the low (but increasing) cluster velocity dispersion. An encounter can trigger the accretion of the reservoirs of cold, rich, and pristine gas located in the halos of single galaxies at $z \gtrsim 2$, continuously replenished by cosmological inflows (Ceverino et al. 2010; Gabor & Bournaud 2014). The accretion of such gas would lower the metallicity, as observed in our sample, and subsequently enhance the SF. In addition, galaxy minor and major mergers could lower the metal abundance themselves (Contini et al. 2012; Queyrel et al. 2012). Moreover, the final cluster potential well in which the galaxies reside and interact can facilitate the merging events through the so-called “gravitational focusing” effect (Martig & Bournaud 2007; Moreno et al. 2013), accelerating the gas accretion from the galaxy outskirts. Recent observational studies have shown an SFR increase and metallicity decrease (up to ~ 0.07 – 0.09 dex) in close pairs and post-mergers in the local universe (Ellison et al. 2013). This result is supported by simulations suggesting that mergers induce the funneling of gas reservoirs from the peripheric regions of galaxies toward the center, diluting the metallicity and triggering new SF (Torrey et al. 2012). This second effect could be effective in terms of gas accretion on galaxies entering the halo of low-redshift clusters, generating an SFR enhancement in the cluster outskirts, as observed for example in Virgo (Temporin et al. 2009). However, given the chemical enrichment due to stellar formation in the last 10 Gyr, the gas accretion might not be effective in reducing the metallicity at low redshift. Deep F140W images of our sample of cluster SFGs in the final stack are shown in Figure 18. Every object shows a disturbed morphology and/or a close companion, which might be a hint of high gas fractions or a close encounter, even if the lack of a redshift determination for the companions does not allow us to draw a robust conclusion (see, e.g., Zanella et al. 2015 for the specific case of ID568, Figure 18, fifth panel). We defer to a future work the detailed study of galaxy morphologies in CL

J1449+0856 and a proper comparison with a morphologically characterized field sample.

The transitional epoch that we have just described could be a key phase for galaxy clusters with the assembly of a substantial fraction of stellar mass in SFGs. In a time interval of 500 Myr, the typical doubling time at $z = 2$ (Daddi et al. 2007) and the typical scale of gas consumption in SFGs (Daddi et al. 2010), each galaxy in our cluster sample would form stars for a total of ~ 3 – $6 \times 10^{10} M_{\odot}$, given the average SFR we measure ($\text{SFR}_{\text{H}\alpha} = 112 M_{\odot} \text{yr}^{-1}$, $\text{SFR}_{\text{SED}} = 73 M_{\odot} \text{yr}^{-1}$). This would double the stellar mass already present in cluster SFGs and increase the overall cluster stellar mass in spectroscopically confirmed members by ~ 15 – 35% in this time interval or, if we extend this reasoning to the past history of the cluster, SFGs could have assembled an important part of the total stellar mass in a relatively short period of time during this phase.

We can gain physical insight about the metal deficiency for cluster SFGs with a simple computation. To explain a 0.15 dex metallicity difference (a factor of $\sim 40\%$), given that $M_{\star} \simeq M_{\text{gas}}$ in MS-SFGs at $z \sim 2$ (Bouché et al. 2007; Daddi et al. 2008), we would need a mass of accreted pristine gas of $2 \times 10^{10} M_{\odot}$ to dilute the metal content of each galaxy. If we assume the presence in the cluster halo of a gas mass-free to cool down and to be dragged and accreted by SFGs in their motion equal to $\sim 15\%$ of the total halo mass ($M_{\text{halo}} = 5 \times 10^{13} M_{\odot}$), the mass accretion rate would be $35 M_{\odot} \text{yr}^{-1}$, assuming a gravitational focusing term $\simeq 5$, a velocity dispersion of 500 km s^{-1} , $R_{200} = 0.4 \text{ Mpc}$, and $R_{\text{gal}} \sim 4 \text{ kpc}$ as a typical SFG radius ($\dot{M}_{\text{acc}} = \rho_{\text{gas,halo}} \cdot \pi R_{\text{gal}}^2 \cdot v_{\text{disp}} \cdot f_{\text{grav}} [M_{\odot} \text{yr}^{-1}]$). However, if we consider only the highest density regions at the core of the cluster ($R_{\text{clu}} \sim 200 \text{ kpc}$), where the gas is likely to collect, the accreted gas mass could rapidly increase by a factor of ~ 8 , enough to halve the metal content of the galaxy. The complementary mechanism linked to galaxy encounters could provide an extra gas accretion rate of $\geq 45 M_{\odot} \text{yr}^{-1}$, considering the galaxy density within the cluster ($\sim 75 \text{ Mpc}^{-3}$ within R_{200}) and a typical distance for a fly-by of 50 kpc ($\dot{M}_{\text{acc}} = M_{\text{res}} \cdot n_{\text{coll}} \cdot f_{\text{grav}} [M_{\odot} \text{yr}^{-1}]$, where n_{coll} is the collision rate and M_{res} the galaxy halo gas reservoir). The reservoirs available in the galaxy outskirts are expected from simulations to be a few $10^9 M_{\odot}$ within a 15 kpc radius around the galaxy (Ceverino et al. 2010; Gabor & Bournaud 2014) and they can be replenished only as long as cold inflows can reach the galaxy, which may not be true once the galaxy enters deeply in the cluster halo. Moreover, we cannot rule out the possibility that the local density may be a more important driver than cluster membership (i.e., large scale environment). Unfortunately, the very low number statistics of cluster SFGs does not allow for a proper comparison among objects within and outside the virial radius to check for the effective influence of the underlying overdensity on the metallicity, neither considering stacked spectra. Future spectroscopic follow-up of the remaining population of spectroscopically confirmed and candidate SF members will be decisive to clarify this complex picture.

6. SUMMARY AND CONCLUSIONS

We have presented the results of the MOIRCS near-IR spectroscopic follow-up of the SF population residing in CL J1449+0856 at $z = 2$. Adding the pre-existing thirteen-band photometry of the field and the deep grism G141 slitless

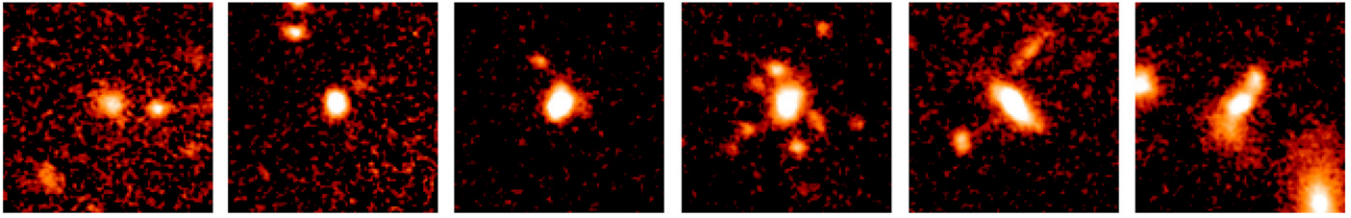


Figure 18. F140W $3'' \times 3''$ ($\sim 25 \times 25$ kpc) cutouts of our sample of cluster SFGs in the mass range $10 \leq \log(M/M_\odot) \leq 11$ (north is up, east is left).

spectroscopy of WFC3, we studied the properties of our sample of cluster SFGs in the mass range of $10 \leq \log(M/M_\odot) \leq 11$ with respect to a mass-matched field sample at comparable redshifts through stacking. In our analysis, we showed the following.

1. The field and cluster samples of SFGs in the studied mass range show comparable $[\text{O III}]/\text{H}\beta$ ratios, but a $\sim 4\sigma$ significant difference in $[\text{N II}]/\text{H}\alpha$ ratios. Using different calibrations of the N2 and O3N2 metallicity indicators, the lower $[\text{N II}]/\text{H}\alpha$ ratio measured in cluster SFGs is translated in a $\sim 0.09\text{--}0.25$ dex (using O3N2_{S14} and N2_{PP04}, respectively) metal deficiency for the objects belonging to the overdensity. The low metallicity value in cluster sources is confirmed using R₂₃ and O₃₂ indicators. Furthermore, it is supported by the low N/O ratio that we measured ($\log(\text{N/O}) = -1.18 \pm 0.15$). The ionization parameter in the cluster stacked sample from R₂₃, O₃₂ ($\mathcal{U} \simeq -2.61$) is higher than typical values for local galaxies, but consistent with other determinations at high redshift.
2. We observe $\sim 4.7\sigma$ significant 2.5 times higher H α luminosity and EW(H α) in the cluster stack, likely due to enhanced sSFR, even if lower dust reddening and/or an uncertain environmental dependence of the continuum-to-nebular emission differential reddening f may play a role. Thus the metal deficiency observed in the cluster sources appears to be correlated with an increase in the SFR with respect to the field; however, we report a $\sim 2.7\sigma$ inconsistency with the prediction of a FMR not evolving up to $z = 2.5$.
3. The nebular lines reddening at $z \sim 2$ is ~ 1.4 times higher than that of stellar continuum estimated through SED fitting, lower than the previous estimates from local measurements and in agreement with recent studies at $z \geq 1.5$ (Kashino et al. 2013; Pannella et al. 2014).
4. Our sample of high redshift galaxies are offset from the local SF sequence on the BPT emission-line diagnostic diagram. This result is in agreement with previous studies at similar redshifts (Erb et al. 2006; Yabe et al. 2012; Steidel et al. 2014; Zahid et al. 2014b, and others), pointing toward a possible evolution with redshift of the physical conditions of the line emitting regions.
5. The metal deficiency in this $z = 1.99$ cluster could be due to the accretion of pristine gas, which might have diluted the metal content. We speculate that the accretion of large galactic scale gas reservoirs facilitated by the gravitational focusing effect may be responsible for the observed low metal abundance in star-forming cluster members.

We acknowledge the constructive comments from the anonymous referee, which significantly improved the content and presentation of the results. F.V., E.D., and A.Z. were supported by grants ERC-StG UPGAL 240039 and ANR-08-JCJC-0008. F.B. and S.J. acknowledge support from the European Research Council through grant ERC-StG-257720. N.A. has been supported by the Grant-in-Aid for the Scientific Research Fund under grant No. 23224005. This work is based on data collected at Subaru Telescope, which is operated by the National Astronomical Observatory of Japan.

APPENDIX A

As noted in Section 3.2, averaging single spectra does not necessarily coincide with averaging spectral derived quantities. The difference between these two averaged trends depends on the relationship between the the fluxes of single lines and the derived quantities. In our case, we have evaluated the impact of this difference on the mean metallicity calculated through the strong line ratio $[\text{N II}]/\text{H}\alpha$ for a population of MS SFGs. Assuming a functional form for the M_\star -SFR relation and the H α -SFR conversion, one can easily convert the stellar mass of a galaxy into its intrinsic H α luminosity and, given an MRR, into the observable H α flux at a fixed redshift. For this exercise, we have used Sargent et al. (2014) MS parametrization as a function of redshift and the standard Kennicutt (1998) relation to pass from H α intrinsic luminosities to SFRs. As an MRR, we have used the observed trend of our overall sample of SFGs given by the SED fitting described in Section 3.1 and shown in Figure 9. Then, we can convert the stellar mass into the gas-phase metallicity using a parametrization of the MZR (or of the FMR if we want to include the effect of the SFR). Here we have used the Zahid et al. (2014a) parametrization, given its simple form. Finally, we need a conversion from gas-phase metallicities to observed line fluxes. We adopt here the Pettini & Pagel (2004) calibration of the $[\text{N II}]/\text{H}\alpha$ ratio, but in principle we could test any other strong-line ratio. All of these relations are somehow scattered and we have adopted the quoted scatters to introduce a Gaussian random noise to make our simple simulation more realistic. Given all of these relations, we simply generate a random sample of masses in an interesting mass range and derive two estimates of the average metallicity. First, we simply compute the average of the single metallicities in mass bins as obtained from the MZR (Z_{av}); then, we compute the mean metallicity in the same mass bins as derivable from an hypothetical stacking of the spectra of single galaxies, namely from the average of single line fluxes (Z_{stack}). Analytically, it can be shown that Z_{av} and Z_{stack} depend on $[\text{N II}]$ and H α fluxes in different ways, so that a priori they

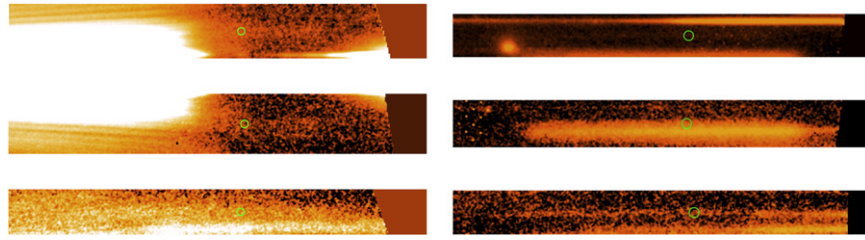


Figure 19. WFC3 G141 slitless spectra of the two cluster candidate members with masses $10 \leq \log(M/M_\odot) \leq 11$ that were not observed with MOIRCS. Left column: ID 424. Right column: ID 660. The three spectra correspond to separate *HST* visits (G13). Green circles mark the expected position of [O III] if the sources were at $z = 1.99$.

can be different:

$$\log \left[\frac{Z_{\text{av}}}{Z_{\text{stack}}} \right] = \log \left(\frac{1}{N} \right) + \log \left[\sum_{i=1}^N \left(\frac{[\text{N II}]}{\text{H}\alpha} \right)_i^{0.57} \right] - \log \left[\left(\frac{\sum_{i=1}^N [\text{N II}]_i}{\sum_{i=1}^N \text{H}\alpha_i} \right)^{0.57} \right] \quad (\text{A.1})$$

where N is the total amount of observed galaxies and 0.57 is the slope of PP04 calibration. Given the parametrizations we adopted, the difference between the two mean estimates decreases with increasing stellar mass. Moreover, averaging the metallicity in smaller mass bins gives rise to smaller differences between Z_{av} and Z_{stack} . Finally, a high number of observed points is more robust against the scatter of the relations we used, reducing the possibility to find huge $\log(Z_{\text{av}}/Z_{\text{stack}})$ ratios in a mass bin. We have stacked sources in a limited high-mass regime ($10 \leq \log(M/M_\odot) \leq 11$) where we have a relatively low number statistics for the cluster sample ($N \sim 10$) and a fairly more robust sample of field galaxies ($N \sim 30$). For a simulated sample of 10 galaxies at $z = 2$ in the mass bin $10 \leq \log(M/M_\odot) \leq 11$, the median difference is $\log(Z_{\text{av}}/Z_{\text{stack}}) = 0.018$ ($\sim 4\%$) with a semi-interquartile range of 0.022 dex over 1000 runs of the simulation. At the same redshift and mass bin but for $N = 30$ observed points, the median difference is reduced to $\log(Z_{\text{av}}/Z_{\text{stack}}) = 0.008$ ($\sim 1\%$) with a semi-interquartile range of 0.005 dex. At these masses the impact of adopting one approach or the other is restrained, but it could be more important at lower masses—due to the steeper MZR—at which the stacking technique is usually widely used.

APPENDIX B

In Figure 19, we show the WFC3 G141 slitless spectra for two candidate members with masses of $10 \leq \log(M/M_\odot) \leq 11$ that were not inserted in MOIRCS masks because of geometrical constraints in slit positioning. Contamination from high orders severely affected these spectra in two of the three *HST* visits, limiting the usable integration time to 4/18 orbits and leading to a higher detection threshold. This did not allow us to detect these intrinsically faint objects (see Section 5.1).

REFERENCES

Abazajian, K. N., Adelman-McCarthy, J. K., Agüeros, M. A., et al. 2009, *ApJS*, **182**, 543
 Alloin, D., Collin-Souffrin, S., Joly, M., & Vigroux, L. 1979, *A&A*, **78**, 200
 Andreon, S., Maughan, B., Trinchieri, G., & Kurk, J. 2009, *A&A*, **507**, 147
 Andrews, B. H., & Martini, P. 2013, *ApJ*, **765**, 140

Asplund, M., Grevesse, N., Sauval, A. J., & Scott, P. 2009, *ARA&A*, **47**, 481
 Baldry, I. K., Glazebrook, K., Brinkmann, J., et al. 2004, *ApJ*, **600**, 681
 Baldwin, J. A., Phillips, M. M., & Terlevich, R. 1981, *PASP*, **93**, 5
 Balogh, M. L., Baldry, I. K., Nichol, R., et al. 2004, *ApJL*, **615**, L101
 Bertin, E., & Arnouts, S. 1996, *A&AS*, **117**, 393
 Birnboim, Y., & Dekel, A. 2003, *MNRAS*, **345**, 349
 Blanton, M. R., Eisenstein, D., Hogg, D. W., Schlegel, D. J., & Brinkmann, J. 2005, *ApJ*, **629**, 143
 Bouché, N., Cresci, G., Davies, R., et al. 2007, *ApJ*, **671**, 303
 Brooks, A. M., Governato, F., Quinn, T., Brook, C. B., & Wadsley, J. 2009, *ApJ*, **694**, 396
 Bruzual, G., & Charlot, S. 2003, *MNRAS*, **344**, 1000
 Calzetti, D., Armus, L., Bohlin, R. C., et al. 2000, *ApJ*, **533**, 682
 Ceverino, D., Dekel, A., & Bournaud, F. 2010, *MNRAS*, **404**, 2151
 Charlot, S., & Longhetti, M. 2001, *MNRAS*, **323**, 887
 Cid Fernandes, R., Stasińska, G., Mateus, A., & Vale Asari, N. 2011, *MNRAS*, **413**, 1687
 Cid Fernandes, R., Stasińska, G., Schlickmann, M. S., et al. 2010, *MNRAS*, **403**, 1036
 Coil, A. L., Aird, J., Reddy, N., et al. 2014, arXiv:1409.6522
 Contini, T., Garilli, B., Le Fèvre, O., et al. 2012, *A&A*, **539**, A91
 Cooper, M. C., Tremonti, C. A., Newman, J. A., & Zabludoff, A. I. 2008, *MNRAS*, **390**, 245
 Cullen, F., Cirasuolo, M., McLure, R. J., Dunlop, J. S., & Bowler, R. A. A. 2014, *MNRAS*, **440**, 2300
 Daddi, E., Bournaud, F., Walter, F., et al. 2010, *ApJ*, **713**, 686
 Daddi, E., Cimatti, A., Renzini, A., et al. 2004, *ApJ*, **617**, 746
 Daddi, E., Dannerbauer, H., Elbaz, D., et al. 2008, *ApJL*, **673**, L21
 Daddi, E., Dickinson, M., Morrison, G., et al. 2007, *ApJ*, **670**, 156
 Davé, R., Finlator, K., & Oppenheimer, B. D. 2012, *MNRAS*, **421**, 98
 Dekel, A., Sari, R., & Ceverino, D. 2009a, *ApJ*, **703**, 785
 Dekel, A., Birnboim, Y., Engel, G., et al. 2009b, *Natur*, **457**, 451
 Dopita, M. A., Sutherland, R. S., Nicholls, D. C., Kewley, L. J., & Vogt, F. P. A. 2013, *ApJS*, **208**, 10
 Dressler, A. 1980, *ApJ*, **236**, 351
 Ellison, S. L., Mendel, J. T., Patton, D. R., & Scudder, J. M. 2013, *MNRAS*, **435**, 3627
 Ellison, S. L., Simard, L., Cowan, N. B., et al. 2009, *MNRAS*, **396**, 1257
 Erb, D. K., Shapley, A. E., Pettini, M., et al. 2006, *ApJ*, **644**, 813
 Fabian, A. C. 1994, *ARA&A*, **32**, 277
 Fakhouri, O., Ma, C.-P., & Boylan-Kolchin, M. 2010, *MNRAS*, **406**, 2267
 Fassbender, R., Nastasi, A., Böhringer, H., et al. 2011, *A&A*, **527**, L10
 Fitzpatrick, E. L. 1999, *PASP*, **111**, 63
 Gabor, J. M., & Bournaud, F. 2014, *MNRAS*, **437**, L56
 Gobat, R., Daddi, E., Onodera, M., et al. 2011, *A&A*, **526**, A133
 Gobat, R., Strazzullo, V., Daddi, E., et al. 2013, *ApJ*, **776**, 9
 Gómez, P. L., Nichol, R. C., Miller, C. J., et al. 2003, *ApJ*, **584**, 210
 Hogg, D. W., Blanton, M. R., Brinkmann, J., et al. 2004, *ApJL*, **601**, L29
 Holden, B. P., Oesch, P. A., Gonzalez, V. G., et al. 2014, arXiv:1401.5490
 Hughes, T. M., Cortese, L., Boselli, A., Gavazzi, G., & Davies, J. I. 2013, *A&A*, **550**, A115
 Ichikawa, T., Suzuki, R., Tokoku, C., et al. 2006, in *Proc. SPIE*, **6269**, 38
 Juneau, S., Dickinson, M., Alexander, D. M., & Salim, S. 2011, *ApJ*, **736**, 104
 Juneau, S., Bournaud, F., Charlot, S., et al. 2014, *ApJ*, **788**, 88
 Kashino, D., Silverman, J. D., Rodighiero, G., et al. 2013, *ApJL*, **777**, L8
 Kennicutt, R. C., Jr. 1998, *ARA&A*, **36**, 189
 Kereš, D., Katz, N., Weinberg, D. H., & Davé, R. 2005, *MNRAS*, **363**, 2
 Kewley, L. J., & Dopita, M. A. 2002, *ApJS*, **142**, 35
 Kewley, L. J., Dopita, M. A., Leitherer, C., et al. 2013a, *ApJ*, **774**, 100
 Kewley, L. J., & Ellison, S. L. 2008, *ApJ*, **681**, 1183
 Kewley, L. J., Maier, C., Yabe, K., et al. 2013b, *ApJL*, **774**, L10

- Kobulnicky, H. A., & Kewley, L. J. 2004, *ApJ*, **617**, 240
- Kodama, T., Tadaka, K.-i., Hayashi, M., et al. 2013, in IAU Symp. 295, The Intriguing Life of Massive Galaxies, ed. D. Thomas, A. Pasquali, & I. Ferreras (Cambridge: Cambridge Univ. Press), 74
- Kriek, M., van Dokkum, P. G., Labbé, I., et al. 2009, *ApJ*, **700**, 221
- Kulas, K. R., McLean, I. S., Shapley, A. E., et al. 2013, *ApJ*, **774**, 130
- Lequeux, J., Peimbert, M., Rayo, J. F., Serrano, A., & Torres-Peimbert, S. 1979, *A&A*, **80**, 155
- Lilly, S. J., Carollo, C. M., Pipino, A., Renzini, A., & Peng, Y. 2013, *ApJ*, **772**, 119
- Magdis, G. E., Daddi, E., Béthermin, M., et al. 2012, *ApJ*, **760**, 6
- Maier, C., Lilly, S. J., Ziegler, B. L., et al. 2014, *ApJ*, **792**, 3
- Maiolino, R., Nagao, T., Grazian, A., et al. 2008, *A&A*, **488**, 463
- Mannucci, F., Cresci, G., Maiolino, R., Marconi, A., & Gnerucci, A. 2010, *MNRAS*, **408**, 2115
- Maraston, C., Pforr, J., Renzini, A., et al. 2010, *MNRAS*, **407**, 830
- Markwardt, C. B. 2009, in ASP Conf. Ser. 411, Astronomical Data Analysis Software and Systems XVIII, ed. D. A. Bohlender, D. Durand, & P. Dowler (San Francisco, CA: ASP), 257
- Martig, M., & Bournaud, F. 2007, SF2A-2007: Proceedings of the Annual Meeting of the French Society of Astronomy and Astrophysics 344, ed. J. Bouvier, A. Chalabaev, & C. Charbonnel
- Masters, D., McCarthy, P., Siana, B., et al. 2014, *ApJ*, **785**, 153
- Moreno, J., Bluck, A. F. L., Ellison, S. L., et al. 2013, *MNRAS*, **436**, 1765
- Mouchine, M., Baldry, I. K., & Bamford, S. P. 2007, *MNRAS*, **382**, 801
- Muzzin, A., Wilson, G., Demarco, R., et al. 2013, *ApJ*, **767**, 39
- Nagao, T., Maiolino, R., & Marconi, A. 2006, *A&A*, **459**, 85
- Neistein, E., & Dekel, A. 2008, *MNRAS*, **388**, 1792
- Noll, S., Pierini, D., Cimatti, A., et al. 2009, *A&A*, **499**, 69
- Osterbrock, D. E., & Ferland, G. J. (ed.) 2006, *Astrophysics of Gaseous Nebulae and Active Galactic Nuclei* (Sausalito, CA: Univ. Sci. Books)
- Pannella, M., Elbaz, D., Daddi, E., et al. 2014, arXiv:1407.5072
- Papovich, C., Momcheva, I., Willmer, C. N. A., et al. 2010, *ApJ*, **716**, 1503
- Peng, C. Y., Ho, L. C., Impey, C. D., & Rix, H.-W. 2002, *AJ*, **124**, 266
- Peng, C. Y., Ho, L. C., Impey, C. D., & Rix, H.-W. 2010, *AJ*, **139**, 2097
- Pérez-Montero, E., & Contini, T. 2009, *MNRAS*, **398**, 949
- Pettini, M., & Pagel, B. E. J. 2004, *MNRAS*, **348**, L59
- Pilyugin, L. S., Grebel, E. K., & Mattsson, L. 2012, *MNRAS*, **424**, 2316
- Queyrel, J., Contini, T., Kissler-Patig, M., et al. 2012, *A&A*, **539**, A93
- Revaz, Y., Combes, F., & Salomé, P. 2008, *A&A*, **477**, L33
- Rodighiero, G., Renzini, A., Daddi, E., et al. 2014, *MNRAS*, **443**, 19
- Rousselot, P., Lidman, C., Cuby, J.-G., Moreels, G., & Monnet, G. 2000, *A&A*, **354**, 1134
- Salomé, P., Combes, F., Revaz, Y., et al. 2011, *A&A*, **531**, A85
- Salpeter, E. E. 1955, *ApJ*, **121**, 161
- Santos, J. S., Fassbender, R., Nastasi, A., et al. 2011, *A&A*, **531**, L15
- Sargent, M. T., Daddi, E., Béthermin, M., et al. 2014, *ApJ*, **793**, 19
- Savaglio, S., Glazebrook, K., le Borgne, D., et al. 2005, *ApJ*, **635**, 260
- Scoville, N., Aussel, H., Brusa, M., et al. 2007, *ApJS*, **172**, 1
- Shapley, A. E., Reddy, N. A., Kriek, M., et al. 2014, arXiv:1409.7071
- Shimakawa, R., Kodama, T., Tadaki, K.-i., et al. 2015, *MNRAS*, **448**, 666
- Stanford, S. A., Brodwin, M., Gonzalez, A. H., et al. 2012, *ApJ*, **753**, 164
- Steidel, C. C., Adelberger, K. L., Shapley, A. E., et al. 2005, *ApJ*, **626**, 44
- Steidel, C. C., Rudie, G. C., Strom, A. L., et al. 2014, *ApJ*, **795**, 165
- Storey, P. J., & Zeppen, C. J. 2000, *MNRAS*, **312**, 813
- Strazzullo, V., Gobat, R., Daddi, E., et al. 2013, *ApJ*, **772**, 118
- Temporin, S., Duc, P.-A., & Ilbert, O. (XMM-LSS/SWIRE Collaboration) 2009, *AN*, **330**, 915
- Torrey, P., Cox, T. J., Kewley, L., & Hernquist, L. 2012, *ApJ*, **746**, 108
- Tremonti, C. A., Heckman, T. M., Kauffmann, G., et al. 2004, *ApJ*, **613**, 898
- Troncoso, P., Maiolino, R., Sommariva, V., et al. 2014, *A&A*, **563**, A58
- Trump, J. R., Konidakis, N. P., Barro, G., et al. 2013, *ApJL*, **763**, L6
- Williams, R. J., Quadri, R. F., Franx, M., van Dokkum, P., & Labbé, I. 2009, *ApJ*, **691**, 1879
- Wuyts, E., Kurk, J., Förster Schreiber, N. M., et al. 2014, *ApJL*, **789**, L40
- Wuyts, S., Labbé, I., Franx, M., et al. 2007, *ApJ*, **655**, 51
- Yabe, K., Ohta, K., Iwamuro, F., et al. 2012, *PASJ*, **64**, 60
- Yan, R., Ho, L. C., Newman, J. A., et al. 2011, *ApJ*, **728**, 38
- Yoshikawa, T., Akiyama, M., Kajisawa, M., et al. 2010, *ApJ*, **718**, 112
- Zahid, H. J., Bresolin, F., Kewley, L. J., Coil, A. L., & Davé, R. 2012, *ApJ*, **750**, 120
- Zahid, H. J., Dima, G. I., Kudritzki, R.-P., et al. 2014a, *ApJ*, **791**, 130
- Zahid, H. J., Kashino, D., Silverman, J. D., et al. 2014b, *ApJ*, **792**, 75
- Zanella, A., Daddi, E., Le Ploc'h, E., et al. 2015, *Natur*, in press
- Zeimann, G. R., Stanford, S. A., Brodwin, M., et al. 2012, *ApJ*, **756**, 115